Available online at www.sciencedirect.com
SCIENCE DIRECT®
Geochimica et Cosmochimica Acta 70 (2006) 3593–3612
Geochimica
www.elsevier.com/locate/gca

Molecular scale investigations of the reactivity of magnetite with formic acid, pyridine, and carbon tetrachloride

Richard S. Cutting [a], Chris A. Muryn [b], Geoffrey Thornton [c], David J. Vaughan [a,*]

[a] *Williamson Research Centre for Molecular Environmental Science, School of Earth, Atmospheric and Environmental Sciences, University of Manchester, Manchester M13 9PL, UK*
[b] *School of Chemistry, University of Manchester, Manchester M13 9PL, UK*
[c] *London Centre for Nanotechnology, Department of Chemistry, University College London, London WC1H 0AJ, UK*

Received 16 November 2005; accepted in revised form 10 April 2006

Abstract

The (111) surface of magnetite, a dominant growth and fracture surface of this mineral, has been studied using Scanning Tunneling Microscopy (STM) at atomic resolution. In line with previous work, this surface shows three possible terminations which can be related to different level slices through the bulk structure. The reactivities of these different surface terminations have been explored by exposing them, under highly controlled conditions, to formic acid, pyridine, and carbon tetrachloride and undertaking further imaging at atomic resolution. These investigations have, themselves, helped to discriminate between competing models of surface structure. The so-called A′ surface termination we now regard as exposing 1/4 monolayer of tetrahedrally coordinated Fe ions over a close packed oxygen layer, and the A surface termination as being these same Fe ions but each capped by a single oxygen. The so-called B surface termination, previously thought to expose 1/2 monolayer of equal numbers of octahedral and tetrahedral Fe ions over a close packed oxygen layer, we now regard as this same arrangement but again with each Fe capped with an oxygen. For all three molecules, the A′ surface is most reactive but the reactions observed are markedly different. Formic acid undergoes dissociation at the magnetite surface, apparently chemisorbing at the A′ surface via a bidentate non-bridging complex. On the same A′ surface, pyridine is chemisorbed through a monodentate linkage via the 'basal' nitrogen of the molecule. For both formate and pyridine, a weaker interaction (a 'physisorption') was observed with the A and B surfaces, interpreted as involving attachment of the intact molecule. The exceptions to this were where the interaction involved chemisorption at defects on A and B type surfaces. The behavior of carbon tetrachloride on the magnetite surface is very different to the other molecules studied. Only the A′ surface is significantly reactive, and the molecule undergoes a series of temperature-dependant dissociation and surface chemical reactions. These involve sorption of intact CCl_4 molecules at the lowest temperatures, dissociation into CCl_2 and Cl species at around room temperature, and removal from the magnetite of surface oxygens to form $OCCl_2$ and then Fe to form $FeCl_2$ at successively higher temperatures. At around room temperature, both strongly bonded Cl atoms and weakly bonded CCl_2 molecules appear to co-exist on the same (A′ type) surface, a situation not previously observed in iron oxide systems.

1. Introduction

Reactions that occur at the surfaces of oxide and oxyhydroxide minerals, particularly those of iron, are of great importance in geochemistry. However, relatively little is known regarding relationships between surface structure and reactivity at the atomic scale, particularly in more complex iron oxide minerals such as magnetite. In the present work, the (111) surface of magnetite, a major growth and fracture surface of this mineral, has been exposed to three representative organic molecules in a highly controlled UHV environment where in situ atomic resolution imaging can be used to study reactivity. Scanning Tunneling Microscope (STM) images have been recorded before and after exposure to high purity vapours of formic acid

* Corresponding author. Fax: +44 0 161 306 9361.
E-mail address: David.Vaughan@manchester.ac.uk (D.J. Vaughan).

0016-7037/$ - see front matter © 2006 Elsevier Inc. All rights reserved.
doi:10.1016/j.gca.2006.04.034

(HCOOH), pyridine (C_5H_5N), and carbon tetrachloride (CCl_4). These molecules were selected on the basis of their variable chemistry on oxide surfaces.

Formic acid was used in the present study as representative of an extremely large and diverse groups of chemicals, the carboxylic acids and their derivatives. The molecule (Figs. 1a and b), possesses an acid proton that forms part of the carboxylate group. Both experimental and theoretical studies of HCOOH adsorption on oxides indicate that the molecule readily undergoes partial dissociation to $HCOO^-$ and H^+ on many surfaces, including rutile TiO_2 (110) (Idriss et al., 1996; Ahdjoudj and Minot, 1997; Chambers et al., 1997; Henderson, 1997; Wang et al., 1997; Bates et al., 1998; Tanner et al., 2002), MgO (100) (Petrie and Vohs, 1991a; Domen et al., 1993), ZnO (0001)-Zn (Petrie and Vohs, 1991b), and SnO_2 (110) (Gercher and Cox, 1994). Typically, the $HCOO^-$ group is adsorbed at Lewis acid (cation) sites, whilst H^+ interacts with basic (oxygen) sites, in some cases leading to the adsorption of OH^- at the surface. The absence of basic surface sites does not preclude the possibility of HCOOH dissociation; formic acid has been shown to dissociate readily on a variety of single crystal metal substrates, including Cu (110) (Silva et al., 1999).

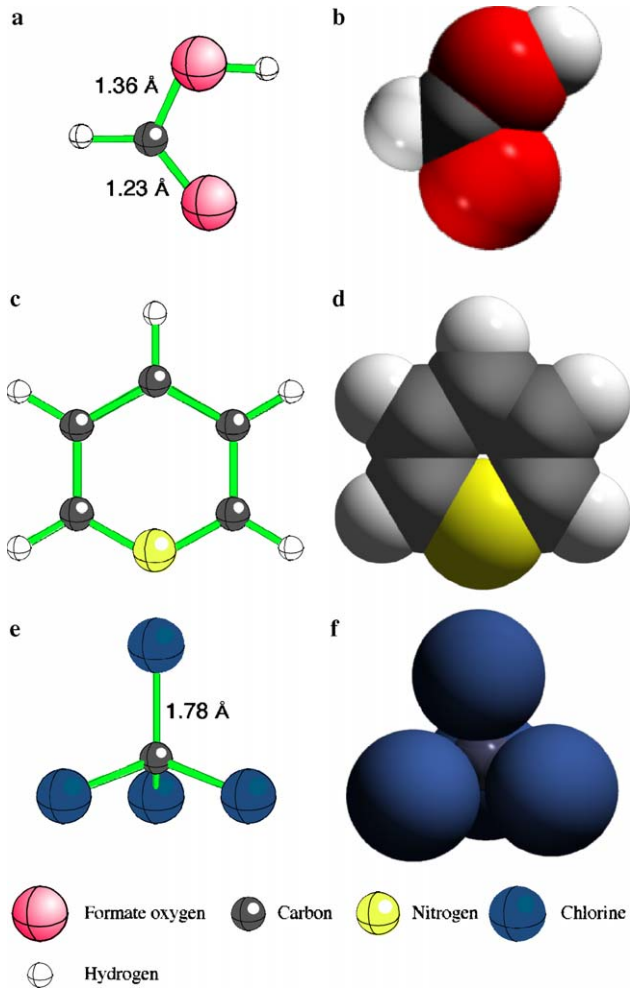

Fig. 1. (a, c, and e) are ball and stick models, and (b, d, and f) are space filling models of formic acid, pyridine, and carbon tetrachloride, respectively.

By contrast, pyridine comprises a benzene ring in which one of the C atoms is replaced by N, as shown in Figs. 1c and d. Interaction of pyridine with oxide surfaces has not been extensively investigated, although Ultraviolet Photoelectron Spectroscopy (UPS) has been used in order to investigate the adsorption of pyridine on ZnO (1100) (Lüth et al., 1978). This study suggests that both the nitrogen lone pair and π orbitals of the C_5H_5N are affected by the formation of a chemisorption bond to the substrate. In addition, other authors have studied pyridine adorption and dynamics on rutile TiO_2 (110) using STM (Suzuki et al., 1998a,b, 1999). These authors note that the condensation of a mobile, physisorbed state occurs initially. This species is subsequently thermally activated at ~350 K, to form either a partially dehydrogenated or chemisorbed species (Suzuki et al., 1998a).

Carbon tetrachloride is a tetrahedral molecule, comprising a single carbon atom bonded to four chlorines, as shown in Figs. 1e and f. Recent auger electron spectroscopy (AES), temperature programmed desorption (TPD), X-ray photoelectron spectroscopy (XPS), and STM investigations of CCl_4 adsorption on the Fe_3O_4 (111) selvedge of α-Fe_2O_3 (0001) indicate that dissociation occurs spontaneously at 100 K, giving rise to adsorbed Cl and CCl_2 (Abib et al., 2002; Camillone et al., 2002; Rim et al., 2002; Abib et al., 2003a,b). Recent work by Rim et al. (2003, 2004) using STM concludes that the adsorption of Cl, produced as a result of the dissociation of CCl_4, is restricted to two distinct active sites on the Fe_3O_4(111) surface. The first of these sites is atop an exposed Fe_{tet1} ion (see further discussion below), whilst the second is located at a threefold oxygen vacancy site generated as a result of O-abstraction during the desorption of phosgene (Rim et al., 2004). A variable temperature STM study indicates that the temperature of the substrate during initial exposure to CCl_4 vapour plays a critical role in determining the resulting populations of Cl species on the surface.

Although the motivation of many previous studies on these systems has been concerned with industrial processes, it is important to emphasise the geochemical significance of this work, and of the new work reported here. For example, it has recently been demonstrated that formic acid can be synthesised on the surfaces of wet silicate minerals due to the photochemical reduction of CO_2 by ultraviolet radiation (Ohta et al., 2002). This may prove a significant factor when considering both the rate and extent of hydrous chemical weathering of geological materials, since the global flux of formic acid produced in this manner is estimated to be greater than 3000 Tga^{-1}. The occurrence of N-heterocyclic compounds like pyridine in the natural environment is also well established (Fetzner, 1998). They perform a variety of biological functions including acting as electron carriers (NAD(P)H and flavine nucleotides), acting as constituents of nucleotides in DNA and RNA,

and as components of molecules such as ATP and GTP that are associated with energy storage. Other naturally occurring *N*-heterocyclic compounds include: pyridoxine (vitamin B_6), various porphyrins, mycotoxins, and melamine (Fetzner, 1998). Furthermore, numerous anthropogenic *N*-heterocyclic compounds occur, derived primarily from pharmaceuticals, dyes, industrial solvents, and pesticides. *N*-heteroaromatic compounds are produced mainly from coal tars that are themselves produced by the low-temperature carbonisation or coking of raw fossil fuel or biomass. In recent decades, global annual production of pyridine, 2-methylpyridine, 3-mythlpyridine, and 4-methylpyridine has been estimated at 26000, 8000, 9000, and 1500 Gga^{-1}, respectively (Shimizu et al., 1993). Owing to their relatively high water solubility and weak sorption to soil and aquifer materials, heteroaromatic contaminants have the potential to be transported readily in subsurface environments, resulting in the contamination of subsoil regions and groundwater. Groundwater contamination by *N*-heterocyclic compounds has been investigated extensively (see Canter and Sabatini, 1994; Hale and Aneiro, 1997).

Carbon tetrachloride and other halogenated organic compounds are also widespread in the natural environment (Klick, 1992). As with formic acid and pyridine, CCl_4, and other polyhalogenated organic compounds have both natural and anthropogenic sources. Studies of deep ocean sediments indicate that, prior to the onset of anthropogenic CCl_4 emission at the beginning of the last century, the atmospheric mole fraction of CCl_4 was $\sim <0.1\times10^{-12}$ (Wallace et al., 1994). A study undertaken in 1998 indicated that the equivalent values had increased to $>100\times10^{-12}$ (Happell and Wallace, 1998). This increase is due primarily to the widespread use of CCl_4 as a chemical feedstock for chlorofluorocarbon production, and as a solvent. Recent evidence suggests that, in addition to well-known atmospheric (Montzka et al., 1996) and deep oceanic sinks (Bullister and Wisegarver, 1998), significant terrestrial sinks for CCl_4, and other halogenated organic compounds exist (Khalil and Rasmussen, 1989).

Studies of the kind reported here, although not performed under ''realistic'' geochemical conditions, inform our understanding of the interactions between organic compounds and mineral surfaces at the molecular scale. Studies of dehydrated mineral surfaces in UHV provide valuable insights into the processes occurring at mineral surfaces on the atomic scale. In addition, the use of organic molecules as chemical probes reveals the heterogeneity of sites present on Fe_3O_4 (111) surfaces and offers insights into the chemical nature of surface sites. Such studies are a prerequisite to an atomic scale understanding of reactions occurring at the surfaces of fully hydrated minerals. Indeed, the data presented here have important implications for understanding the formation and evolution of hydrated surfaces since H_2O is likely to adsorb dissociatively at sites that expose uncapped Fe ions. The present work may also have relevance to cosmochemical studies aimed at understanding the role of surface mediated reactions (in UHV) in the fractionation of the interstellar medium.

2. Experimental

All measurements reported here were made using a UHV Variable Temperature Scanning Tunnelling Microscope (Omicron GmbH, Germany) operating in ''constant current mode''. This is the most widely used mode of operation employed for STM experiments (Binnig and Rohrer, 1982). It refers to the use of a feedback loop in order to vary the voltage applied to the piezo tube and, thus, the tip-sample separation, such that the tunneling current is maintained constant (Wiesendanger, 1994). The system comprises a sample preparation chamber and an analysis/STM chamber, separated by a manual gate valve. Both chambers are equipped with an ion gun and a manipulator for transferring and heating samples by electron bombardment. In addition, both chambers are equipped with two gas lines for the introduction of gases and vapours into the vacuum and a quadrupole mass spectrometer for residual gas analysis. The analysis chamber is also equipped with four-grid optics for conducting low energy electron diffraction (LEED) measurements and an auger electron spectroscopy (AES) facility. The base pressure of the analysis/STM chamber was $<5\times10^{-11}$ mbar. The instrument was calibrated by measuring twenty monatomic steps (and multiples thereof) on a reconstructed Cu (110)-(2×1)O surface. The measured step heights were averaged and the error determined by comparison with step height values determined using X-ray diffraction. This yields a total error of 0.2 Å, giving an uncertainty in step height determination of ±0.1 Å.

The naturally occurring magnetite sample used here was obtained from the Kola Peninsula, Russia and exhibited a well-developed octahedral habit. A $6\times3\times1$ mm^3 wafer was cut parallel to a large (111) growth face. A sample of material obtained during cutting and polishing was examined using X-ray powder diffraction which showed only magnetite to be present. The wafer was subsequently polished to within 0.5° of a (111) plane, as determined by Laue back reflection. Following introduction to the UHV chamber, the surface was prepared by several cycles of in situ cleaning involving Ar^+ ion bombardment (1 kV) for 15 min at 298 K, followed by annealing at either 1023 or 1173 K for 45 min in UHV. Varying the annealing temperature in this manner allows deductions to be made regarding the relative stability of the various surface terminations. The temperature of the crystal was monitored using a calibrated K-type thermocouple and an optical pyrometer.

Formic acid (*Fisher Scientific* 99%), pyridine (*VWR* 99%), and carbon tetrachloride (*VWR* 99%) were introduced into a glass dosing-vial and purified prior to use by successive freeze-thaw-pump cycles. The purity of the vapour in the gas line was monitored using a quadrupole mass spectrometer. Separate isothermal adsorption experiments were carried out in conjunction with atomic resolution STM

imaging. In each case, a clean Fe_3O_4 (111) surface was exposed to controlled amounts of formic acid, pyridine or carbon tetrachloride vapour. The same region of the surface imaged prior to exposure was subsequently re-imaged after dosing. In practice, this was achieved by halting the scan, disabling the feedback loop and withdrawing the tip ~140 nm from the surface using the fine motion controls in the software. Verification that the same area of the surface was imaged before and after dosing was obtained by tracking characteristic patterns of point defects, or a given irregularity in a step edge, apparent in both images. This approach allows sorbate-induced changes of the substrate to be unambiguously identified. In addition, clean Fe_3O_4 (111) surfaces were exposed to CCl_4 vapour and subsequently rapidly heated to 673 K and the temperature held constant for three minutes. This process, commonly termed "flash annealing" enabled the assessment of chlorine mobility within this temperature range.

3. Results and discussion

Following several cycles of Ar^+ ion bombardment and annealing at 1123 K for 45 min in UHV, a sharp hexagonal (1×1) LEED pattern, similar to that reported in previous investigations (Weiss et al., 1993; Barbieri et al., 1994; Lennie et al., 1996; Kim et al., 1998; Joseph et al., 1999a,b; Ritter and Weiss, 1999; Shaikhutdinov et al., 1999, 2000; Fellows et al., 2000; Camillone et al., 2002; Abib et al., 2003b) was obtained for the Fe_3O_4 sample. Large area STM images of this surface shown in Fig. 2 reveal the existence of three distinct kinds of surface (labeled A, A′, and B). The step height down from an A to an A′ surface is 1.2 ± 0.1 Å, and from an A′ to an A surface is 3.7 ± 0.1 Å. The step height down from the A surface to the B is 4.5 ± 0.1 Å, that from termination B down to A is 0.4 ± 0.1 Å. The 1.2 ± 0.1 Å step down from an A-type to an A′-type surface has not been reported previously, and the other measured step heights are in good agreement with published values (Lennie et al., 1996). Summation of the three step heights yields a value of 4.9 ± 0.1 Å, which is in good agreement with the repeat distance of 4.85 Å in the [111] direction in bulk Fe_3O_4 (see Fig. 3). This value is also in good agreement with the height of 4.8 Å measured using STM for single crystal Fe_3O_4 (111), thin film Fe_3O_4 (111) (Weiss et al., 1993; Kim et al., 1998; Joseph et al., 1999b; Shaikhutdinov et al., 1999, 2000) and reduced α-Fe_2O_3 (0001) (Fellows et al., 2000).

Higher resolution images of these three kinds of surface are shown in Figs. 4a, b, and c, with corresponding models derived from the bulk structure of magnetite shown in Figs. 4d, e, and f. The suggested positions of bright features in the STM images are marked with "X" on both figures. Higher resolution imaging of A and A′ surfaces (see Figs. 4a and b, respectively) reveals close packed arrays of bright features separated by 6.0 ± 0.5 Å. Based on previous interpretations of STM images of this surface (Voogt et al., 1996; Weiss, 1997; Kim et al., 1998; Shaikhutdinov et al., 1999, 2000; Weiss and Ranke, 2002), we assume that each bright feature on an A′ surface represents a single iron atom, such that the surface exposes 1/4 monolayer of Fe_{tet1} ions over a close packed O layer (see Fig. 4e). This interpretation is supported by recent ab initio periodic Hartree-Fock electronic structure calculations performed by Ahdjoudj et al. (1999). These calculations indicate that a symmetrical slab, corresponding to the stacking sequence $FeO_4Fe_3O_4Fe$ offers greatest stability since the dipole moment is zero. Such a slab exposes a single monolayer of Fe_{tet1} ions over a close packed oxygen layer, which is consistent with the structure of A′ surfaces proposed here. The stability of the slab is further increased by strong vertical displacement of the underlying O atoms, such that the structure agrees with earlier models predicted on the basis of Low Energy Electron Diffraction current-voltage (LEED I-V) studies (Weiss et al., 1993). It should be noted that Lennie et al. (1996) originally proposed that the A′ surface exposes a trimer of uncapped Fe_{oct1} ions but, for reasons explained below, we no longer favour this model.

For A-type surfaces it is proposed that the Fe_{tet1} ions are capped by an O atom (see Fig. 4d). The measured step height of 1.2 ± 0.1 Å and lateral registry of features across a step down from an A to an A′ surface is consistent with the absence of a capping O ion in the case of the latter. By contrast, surface B exposes a hexagonal array of bright features separated by 3.6 ± 0.5 Å (see Fig. 4c). It has been proposed that surface B exposes 1/2 monolayer of Fe_{oct1} and Fe_{tet1} ions over a close packed oxygen layer and, therefore, that it is individual Fe_{oct1} and Fe_{tet1} ions that give rise to the bright features in Fig. 4c. However, the unreactive

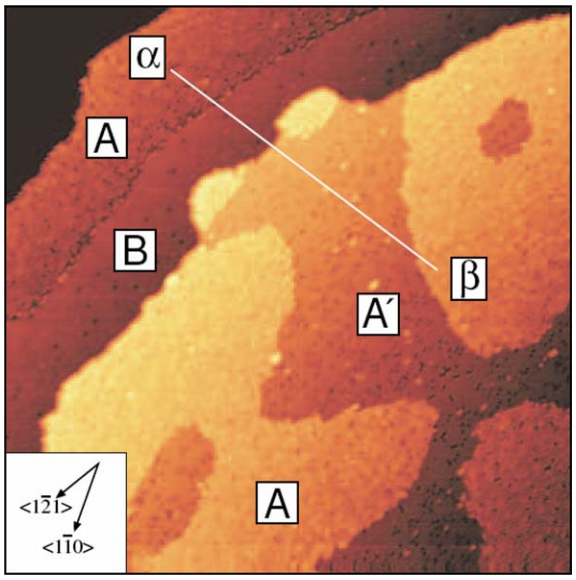

Fig. 2. 1000×1000 Å^2 constant current (2.0 V, 1.0 nA) STM image of an Fe_3O_4 (111) surface following Ar^+ ion bombardment for 15 min at 298 K and annealing at 1123 K for 45 min in UHV. In this and all subsequent figures showing STM images, the crystallographic directions of the substrate are indicated. The line α–β relates to a cross section shown in Fig. 3.

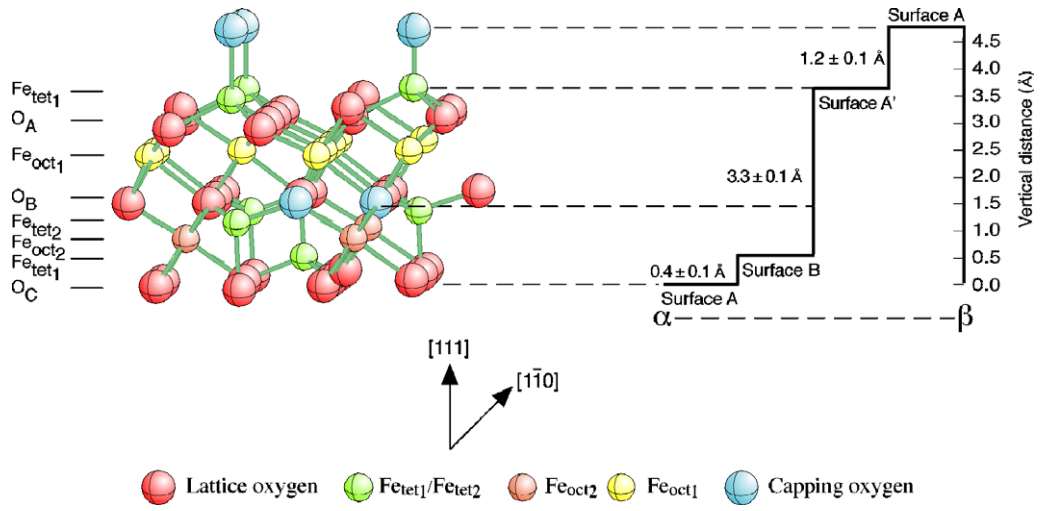

Fig. 3. The bulk structure of magnetite emphasizing the layers of atoms parallel to the (111) plane. Atom layers parallel to the (111) plane are labeled on the left hand side of the figure, and the level slices approximating to the three proposed alternative surface terminations (A, A′, and B) are shown on the right hand side of the figure. The latter also relate to the cross section α–β in the STM image of Fig. 2.

nature of surface B, described in detail below, leads us to suggest that these iron atoms are also each capped by an oxygen atom, and it is these oxygens which are being imaged (as shown in Fig. 4f).

3.1. Exposure to formic acid

Fig. 5 shows 500×500 Å^2 STM images of the same area of a Fe_3O_4 (111) surface both before (a) and immediately after (b) exposure to 4.0×10^{-6} mbarsec of HCOOH vapour at 298 K. In the latter image, numerous bright features attributable to adsorbates appear on both the A′ and A surfaces. In the case of A-type surfaces, repeated scanning leads to the migration or desorption of adsorbates. The horizontal lines in Fig. 5b, parallel to the scan direction, suggest mobility of adsorbates under the STM tip (Suzuki et al., 1999). Fig. 6 is a 500×500 Å^2 STM image of an adjacent area after HCOOH exposure and following repeated scanning for approximately 12 min. The lower region of the A-type surface in Fig. 6 (below the dashed white line) has been almost entirely "stripped" of adsorbate groups, whilst adsorbates on the adjacent A′ surfaces remain unaffected by repeated scanning. A relatively small population of immobile adsorbates is evident on A-type surfaces following repeated scanning, as indicated by the use of white circles in Fig. 6. The differences in formate mobility on different terminations suggests that formic acid interacts much more strongly with A′ than A surfaces, forming an immobile species on the former. This is consistent with the interpretations noted above, since it is proposed that A′ surfaces are metal terminated whilst A surfaces are oxygen-terminated. As detailed above, this is supported by the work of previous authors who have demonstrated that, at room temperature, HCOOH molecules dissociate heterolytically on a number of metal-terminated transition metal oxide surfaces. The $HCOO^-$ ion is a strong Lewis base and is expected to interact with Lewis acids (cation sites), whereas one might expect H^+ to combine with oxygen in the substrate giving rise to adsorbed OH. However, in many cases, hydroxyl groups are not adsorbed at room temperature on metal oxide surfaces (Onishi and Iwasawa, 1994a,b).

The limited number of exposed Lewis acid (cation) sites on A-type surfaces may give rise to the high mobility of adsorbates on these surfaces relative to A′-type surfaces. This is consistent with results of an earlier XPS study of HCOOH adsorption on ZnO (0001) (Lindsay et al., 2002). In this case, the partial dissociation of HCOOH to $HCOO^-$ and H^+ was restricted to point defects on terraces and at step sites, both of which expose underlying Zn^{2+} cations. Similarly, it is proposed that the dissociation of formic acid to yield formate and a proton is restricted to point defects on A-type surfaces of Fe_3O_4 (111). This model accounts for the presence of a small population of immobile adsorbates on the A surface, as imaged in Fig. 6. If this is correct, the mobile species imaged on A-type surfaces correspond to adsorbed molecular formic acid. The interaction with non-defective sites on A-type surfaces probably arises as the result of physisorption under the conditions employed here. Whether surface diffusion occurs in the absence of scanning is unclear. However, it is proposed that species that are clearly mobile during imaging diffuse or migrate along atomic rows on A surfaces until a point defect is encountered. The presence of exposed Fe cations at such sites facilitates the partial dissociation of formic acid to formate. The resulting formate groups form a species that is immobile during scanning, as seen in Fig. 6.

Images containing termination B indicate an extremely limited interaction between formic acid vapour and this type of surface (see Fig. 7). As noted above, this result is surprising since B-type surfaces have been thought to terminate in 1/2 monolayer of $Fe_{oct\,2}$ and Fe_{tet1} ions (Lennie et al., 1996). Here, we propose that these iron atoms are each capped by a single oxygen atom, and that it is this atom we are seeing as

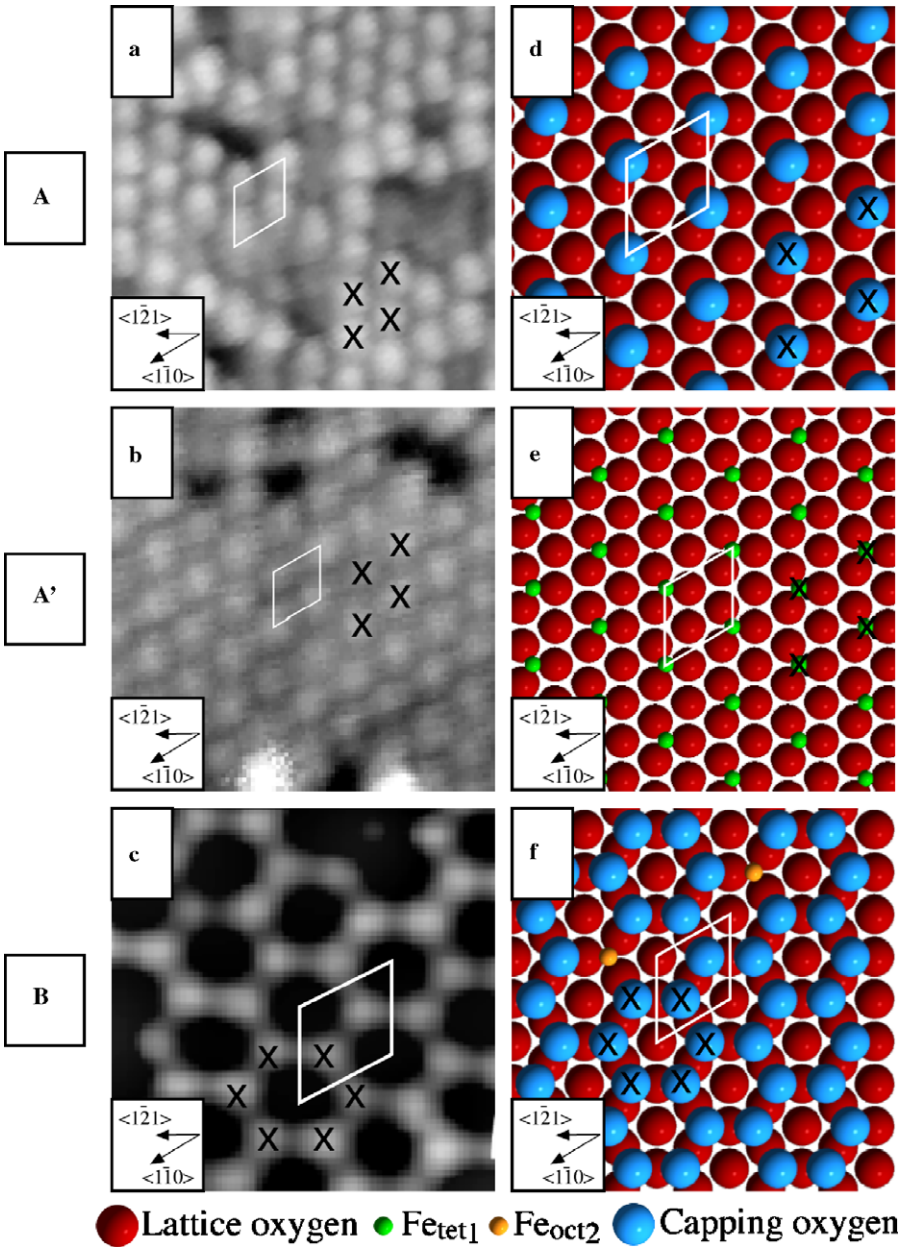

Fig. 4. Higher resolution STM images of (a) termination A (100×100 Å^2) (1.97 V, 1.00 nA), (b) termination A′ (120×120 Å^2) (2.00 V, 1.00 nA), and (c) termination B (16×16 Å^2) (2.00 V, 1.00 nA) with (d, e, and f) showing space filling models for the proposed atomic arrangements giving rise to terminations A, A′, and B, respectively. Several bright protrusions evident in STM images are marked "x", the corresponding atomic positions are indicated on the accompanying space filling models.

bright spots in the STM image. In line with this argument, any immobile adsorbed species on B surfaces appear limited entirely to sites thought to correspond to point defects prior to exposure. These sites often appear in the same position, that is at the site occupied by $Fe_{oct\,2}$ ions in bulk Fe_3O_4. This is also consistent with an observation of Lennie et al. (1996); namely that, although they did not actually study the reactivity of these surfaces, they did note that vacuum contaminants are relatively rare on B surfaces and, when present, always occur at point defects.

Higher resolution images of different terminations of Fe_3O_4 (111) surfaces were also obtained following exposure to formic acid vapour, sufficient to deduce the precise position and height of the adsorbed formate molecule with respect to the features in the underlying substrate. Fig. 8a is a 100×100 Å^2 STM image of an A′-type surface where coverage is sufficiently low that isolated adsorbates occur. This allows the association of a single adsorbate molecule with a single substrate 'protrusion' to be observed directly. On A′ surfaces, the adsorbed formate molecules appear elliptical in shape, with the long axes of individual adsorption related features aligned parallel to one or other of the three atomic row directions, i.e., [110], [101], or [011]. Analysis of these high resolution images shows that adsorbed

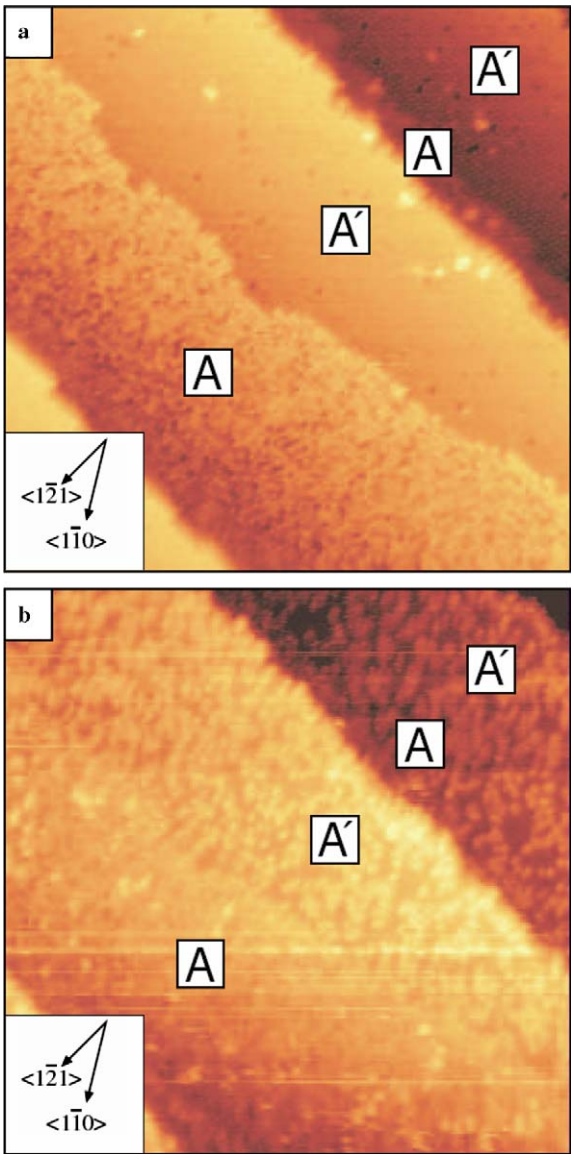

Fig. 5. (a) 500×500 Å^2 constant current (1.90 V, 0.98 nA) STM image of a clean Fe_3O_4 (111) surface after Ar^+ ion bombardment for 15 min and annealing at 1123 K for 45 min in UHV; (b) the same region of the surface following exposure to 4.0×10^{-6} mbarsec of HCOOH.

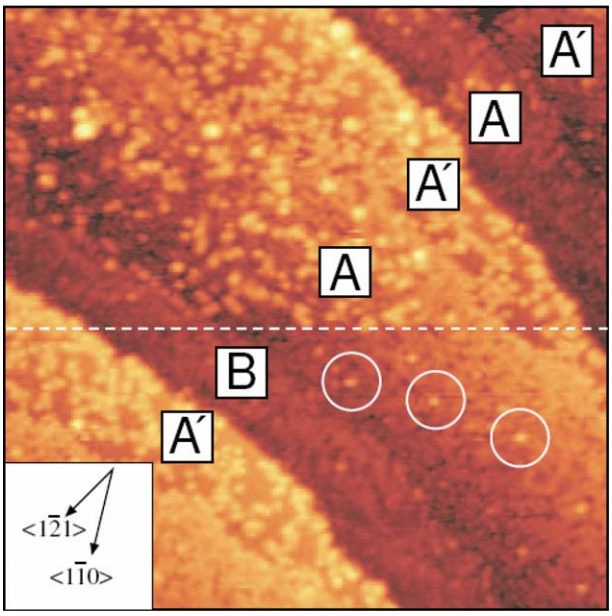

Fig. 6. 500×500 Å^2 constant current (2.11 V, 1.0 nA) STM image of Fe_3O_4 (111) approximately 12 min after exposure to 4×10^{-6} mbarsec of formic acid vapour at 298 K. The dashed white line indicates the upper boundary of previous scans. The white circles indicate examples of formate groups that remain on an A surface after repeated scanning.

molecules sit slightly off-centre with respect to the central axis of atomic rows, parallel to the plane of the surface. No exceptions to this one-to-one association between substrate features and adsorbed formate groups were observed. It is on the basis of evidence such as this that we no longer favour the model for A′ surface structure proposed by Lennie et al. (1996). If A′-type surfaces do expose a trimer of uncapped Fe_{oct1} ions, as proposed by Lennie et al. (1996), then one would expect to observe the association of more than one adsorbed group with a single surface protrusion in some cases. No evidence of this was found; individual adsorbates were always associated with a single surface site on A′ surfaces. Fig. 8b is a line profile taken along the transect α–β in Fig. 8a; it shows that the height of an isolated formate group is 1.7 Å. The characteristic 6.0 Å separation of protrusions associated with Fe_{tet1} ions is again evident, as is a vacant point defect to the right of the formate group in Fig. 8b. These vacant sites are thought to represent missing Fe_{tet1} ions on an A′-type surface and are not expected to interact with formate, owing to their reduced Lewis acidity relative to surrounding sites.

In all cases, adsorption-related features appear bright in constant current STM images obtained at ~+2.0 V. Following arguments presented by previous authors (Onishi and Iwasawa, 1994c), it seems likely that tunneling occurs between occupied states in the tip and unoccupied states of the adsorbed formic acid/formate groups. SCF calculations indicate that the free $HCOO^-$ anion has several unoccupied states, the 2_{b1} (LUMO) at 11.2 eV, 7_{a1} at 15.3 eV, and 5_{b2} at 15.5 eV below vacuum level (E_{vac}) (Peyerimhoff, 1967). It is likely that under these conditions tunneling involves the 2_{b1} molecular orbital. It should be noted, however, that hybridization of the molecular orbitals and surface states near the Fermi Level will occur upon adsorption. This will give rise to unique energy levels that are reduced in energy relative to the molecular orbitals associated with the free formate anion.

In bulk magnetite, two distinct Fe (111) layers exist (see Fig. 3). The first comprises only octahedral (Fe_{oct1}) ions, whereas the second comprises both octahedral and tetrahedral iron atoms. In the first of these two layers, the lateral separation between Fe_{oct1} ions is 2.968 Å. This is similar to that observed for fivefold coordinated Ti cations parallel to the [001] direction on rutile TiO_2 (110) surfaces, and where it is widely accepted that formate groups form a bidentate bond with the surface, bridging two Ti cations (Onishi and

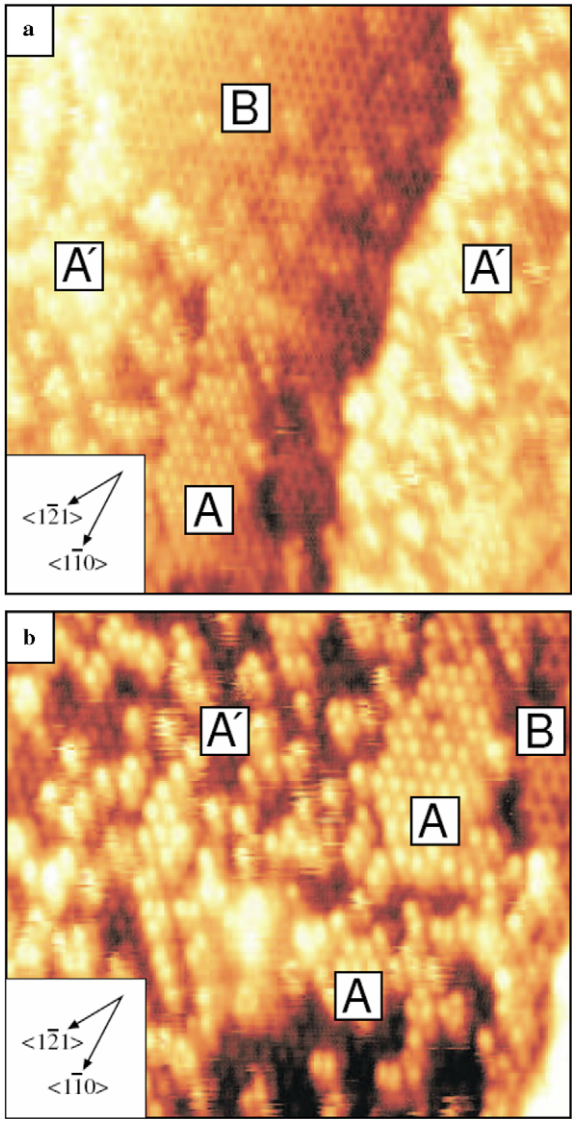

Fig. 7. (a) 250×250 Å^2 constant current STM image (1.86 V, 1.00 nA) and (b) 200×200 Å^2 constant current STM image (1.86 V, 1.00 nA) of Fe_3O_4 (111), following exposure to 2.0×10^{-6} mbarsec of formic acid vapour at 298 K.

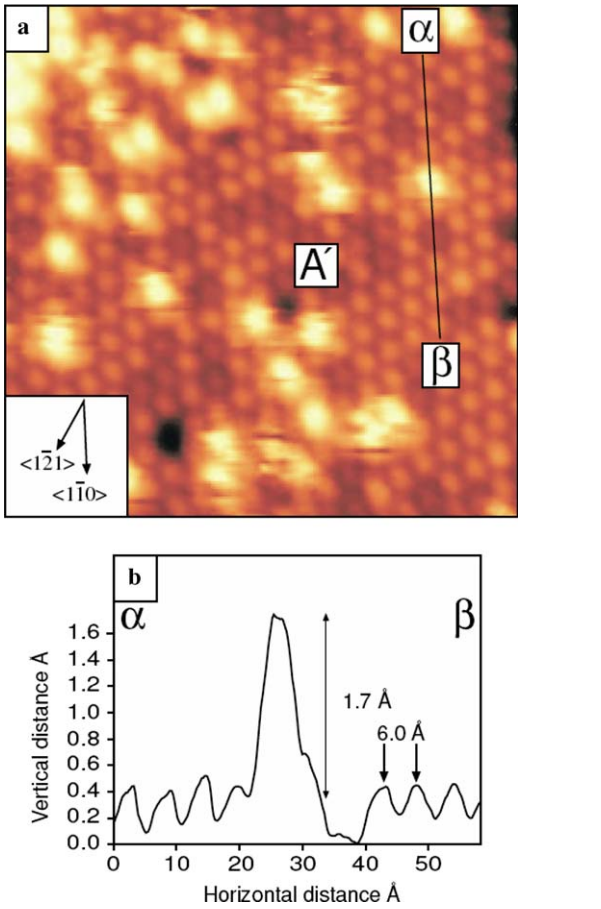

Fig. 8. (a) 100×100 Å^2 constant current (2.04 V, 0.52 nA) STM image of Fe_3O_4 (111), following exposure to 2.5×10^{-7} mbarsec of HCOOH vapour at 1×10^{-7} mbar and 298 K. (b) Line profile taken along transect α–β indicated in (a).

Iwasawa, 1994a,b,c). In Fig. 9, various possibilities for the bonding of the formate group with surface cations of magnetite are shown, with the bidentate bridging configuration shown in Fig. 9a. In the model for A′ surfaces (Weiss et al., 1993; Barbieri et al., 1994; Ritter and Weiss, 1999) discussed above (see Fig. 4e), images are interpreted as arising from a 1/4 monolayer of Fe_{tet1} ions over a close-packed oxygen layer. Here, the lateral separation between Fe_{tet1} cations is 5.92 Å. On the Zn-terminated ZnO (0001) surface, dissociative adsorption of formic acid occurs readily at regular surface sites in a monodentate bonding configuration, as determined using high resolution electron energy loss spectroscopy (HREELS) (Petrie and Vohs, 1991b). The authors relate this observation to the separation of exposed cations at the surface. The O–O distance of the free formate group is 2.25 Å (Zachariasen, 1940), whilst the separation of Zn cations on the ZnO (0001) surface is 3.25 Å (Preuss et al., 1974). The formate group is incapable of bridging the 3.25 Å between two Zn cations although it is capable of bridging the 2.968 Å gap between adjacent fivefold Ti cations on a rutile TiO_2 (110) surface. This indicates some flexibility within the formate molecule, but it is very unlikely that the formate group could bridge the 5.92 Å gap between adjacent Fe_{tet1} cations thought to comprise A′-type surfaces. Thus, adsorbed formate groups would be restricted to either a bidentate, non-bridging configuration (Fig. 9b) or a monodentate configuration (Fig. 9c).

As noted above, adsorbed formate groups appear asymmetric in STM images with the long axes aligned parallel to the principal crystallographic directions of the underlying substrate. Hence, it is proposed that formate groups bond to Fe_{tet1} ions on A′ surfaces in a bidentate, non-bridging configuration (see Fig. 9b). A monodentate configuration is discounted as it has been demonstrated that monodentate formates yield asymmetric shapes in line profile (Iwasawa et al., 1999). Our atomic resolution images of adsorbed formate show, in all cases, a symmetric line profile. This model can explain all of the STM observations reported

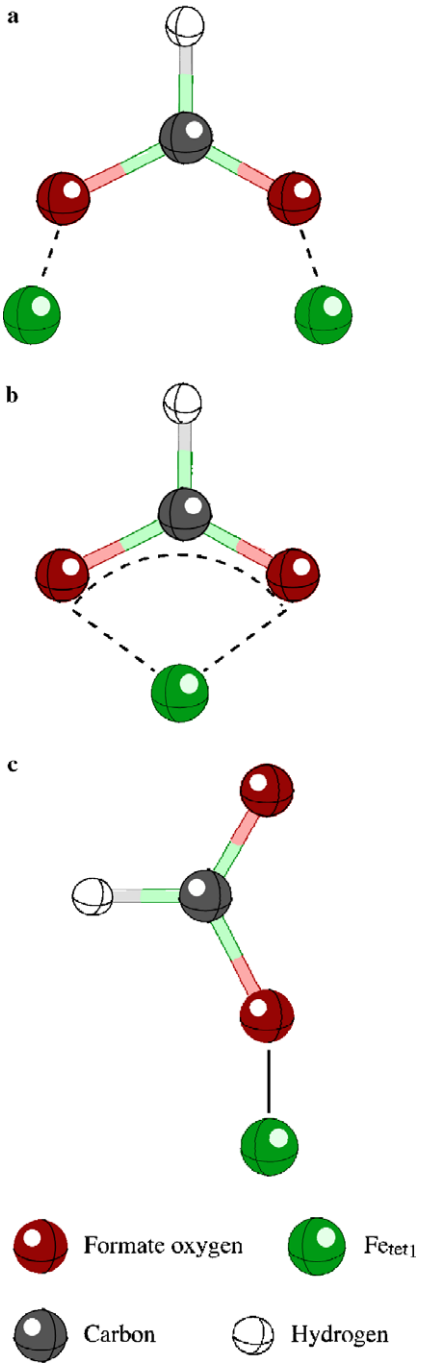

Fig. 9. (a) Ball and stick model of a formate group in a bidentate bridging configuration, (b) in a non-bridging bidentate configuration and (c) in a monodentate configuration.

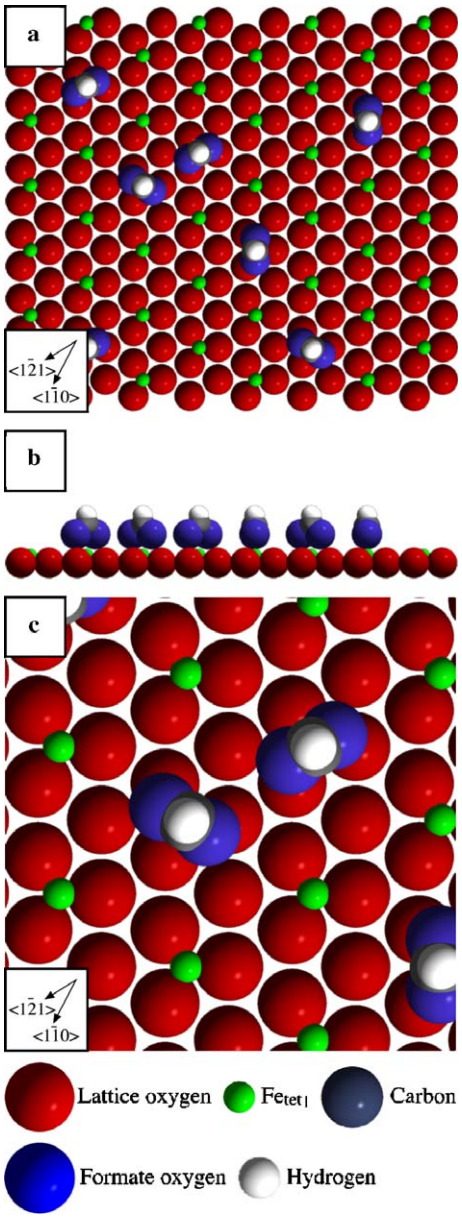

Fig. 10. (a) Top view of a space filling model representing low coverage adsorbed formate on an A′-type surface of Fe_3O_4 (111), (b) side view, (c) top view magnified.

above. For example, that individual formate groups do not exhibit a round shape as on TiO_2 (110) but appear elliptical in shape with the long axes aligned parallel to the atomic rows of the substrate. The orientation of a formate group in a bidentate non-bridging configuration is consistent with the observation of an elliptical shape in the resulting STM image. A model for formate groups adsorbed on A′ surfaces is shown in Fig. 10. The observation that many formates appear as "blurred" or "scratched" features in STM images suggests movement of the adsorbate during imaging, even though repeated scanning of the same region of the surface suggests that individual formate groups are immobile on A′-type surfaces with respect to a given site. This can also be accounted for by the proposed model, since the formation of a bidentate non-bridging complex means that the adsorbed formate group may tilt with respect to an atomic row, parallel to the principal crystallographic directions of the Fe_3O_4 (111) substrate. Such motion may account for the observed "blurring" of adsorbates evident in STM images, even though individual formate groups remain bound to the same surface site during repeated scanning. Furthermore, tilting of the molecule due to the influence of the scanning tip could account

for the observation of formate groups that appear to sit off-axis with respect to an underlying atomic row.

The type of structure we expect to find on A surfaces (see Fig. 4d) as against A′ surfaces (see Fig. 4e) can also be considered. The number of dangling bonds on an A surface is decreased by 2 per (1×1) surface unit cell (Lennie et al., 1996); thus we would expect A-type surfaces to be less reactive than A′-type surfaces. Although adsorption-related features are evident on A-type surfaces following exposure to formic acid vapour at 298 K, such features are often highly mobile under the experimental conditions employed. The only exception to this is a relatively small population of immobile adsorbates, thought to be formate and indicated with the use of white circles in Fig. 6. These features persist at a given surface site during repeated scanning. Careful analysis of consecutive images suggests that these sites correspond to the locations of point defects; using the model proposed above, these would represent oxygen vacancies (see Fig. 4d).

3.2. Exposure to pyridine

Fig. 11a is a 500×500 Å^2 STM image of a clean Fe_3O_4 (111) surface and Fig. 11b is the same surface immediately after exposure to 1.2×10^{-6} mbarsec of pyridine vapour at 298 K. This surface is decorated with numerous bright features, each of which is attributed to an adsorbed pyridine molecule. As with formic acid, these features are considerably more abundant on A′ surfaces than on the A and B surfaces. Several adsorbates on a B termination are indicated in Fig. 11b, using white circles. Fig. 12 is an STM image of the same region obtained approximately 8 min after initial exposure to pyridine vapour. White circles indicate the positions on the B surface that were occupied by adsorbates in Fig. 11b; these features are absent in Fig. 12, presumably due to either the lateral migration of adsorbates on the surface or desorption under the influence of the tip during scanning. This suggests that pyridine is only weakly bound on B surfaces relative to A′ surfaces. Inspection of Figs. 11a,b and 12, indicates that the positions occupied by adsorbates on B surfaces are always associated with sites that expose defects prior to exposure. Furthermore, the removal of adsorption related features from B surfaces (Fig. 12) shows that point defects observed prior to exposure persist after desorption.

Unlike the adsorbates imaged on both B and A′ surfaces, those imaged on A-type surfaces appear as "blurred" or "scratched" fragments. This can be seen in Fig. 13, an STM image that contains both an A and an A′-type surface, separated by a step. Adsorption related features are largely confined to the A′ surface, forming an immobile species, whereas adsorbates on A surfaces are far less abundant and are always imaged as "scratched" fragments. This prevents determination of both the height of the adsorbed species and the precise nature of the active site for adsorption. This type of image has been observed previously in the case of rutile TiO_2 (110) surfaces exposed to pyridine

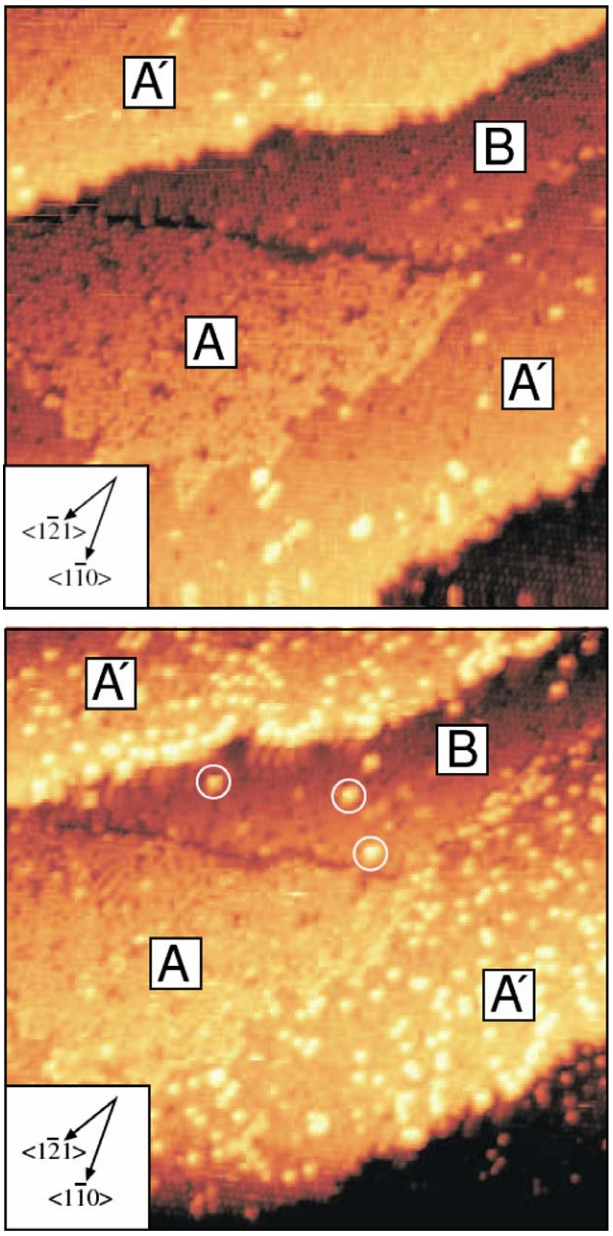

Fig. 11. 500×500 Å^2 constant current (2.0 V, 1.1 nA) STM images of Fe_3O_4 (111) both (a) before and (b) after exposure to 1.2×10^{-6} mbarsec of pyridine vapour at 1×10^{-7} mbar and 298 K.

vapour at 300 K (Suzuki et al., 1999). On the basis of additional TPD and XPS data and theoretical calculations, these authors attribute the "scratched" adsorbates in their STM images to a highly mobile physisorbed species (Suzuki et al., 1998b).

In order to determine the adsorption site of pyridine on A′ surfaces, high-resolution images of immobile adsorbates were obtained at relatively low coverages. Fig. 14a is a 200×200 Å^2 STM image of an A′ surface following exposure to pyridine vapour at 298 K. The image indicates that an adsorbed molecule sits atop of a single bright protrusion associated with the underlying substrate. In addition, adsorbates are in lateral registry with the atomic rows of the substrate, parallel to [110], [011], and [101]

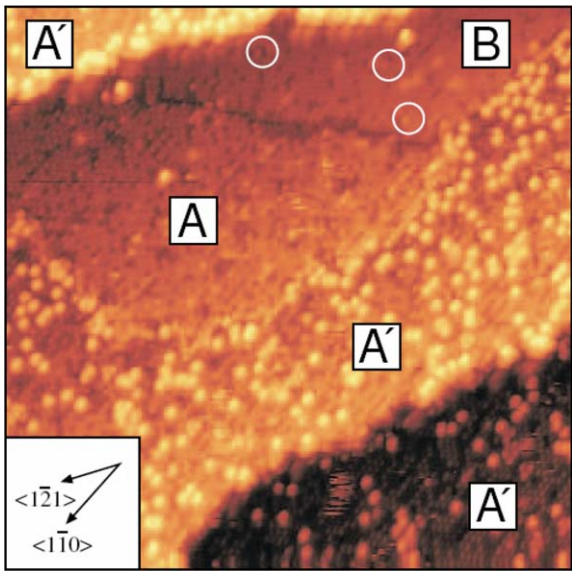

Fig. 12. 500×500 Å^2 constant current (2.0 V, 1.1 nA) STM image of Fe_3O_4 (111) following exposure to 1.2×10^{-6} mbarsec of pyridine vapour at 1×10^{-7} mbar and 298 K. White circles indicate the former positions of three adsorption related features on the B surface seen in Fig. 11.

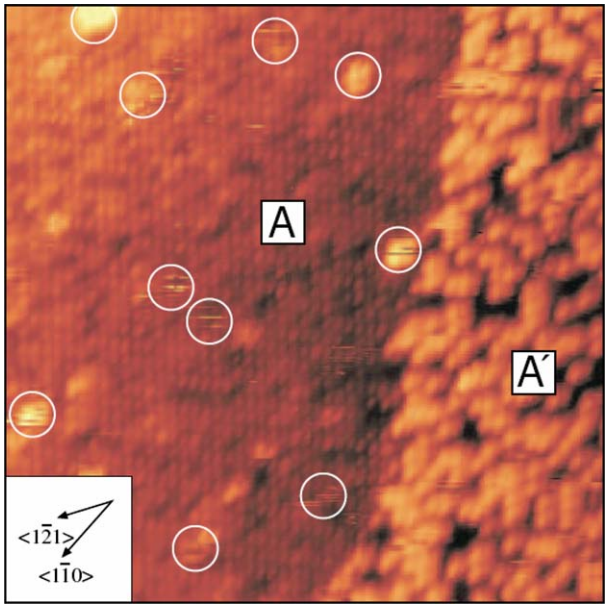

Fig. 13. 300×300 Å^2 constant current (2.1 V, 1.0 nA) STM image of Fe_3O_4 (111) following exposure to 2.2×10^{-6} mbarsec of pyridine vapour at 1×10^{-7} mbar and 298 K. White circles indicate the positions of adsorption related features on the A surface that are imaged as "scratched" fragments.

crystallographic directions. As described above, on A′ surfaces each protrusion is thought to arise from the presence of 1/4 of a monolayer of Fe_{tet1} ions, separated laterally by 6.0 Å. Fig. 14b is a line profile taken along the transect labelled α–β in Fig. 14a; this shows that the height of an adsorbed pyridine on an A′-type surface is 2.4 ± 0.1 Å, which is consistent with the measured value for the same species on TiO_2 (110) (Suzuki et al., 1998a,b,c, 1999).

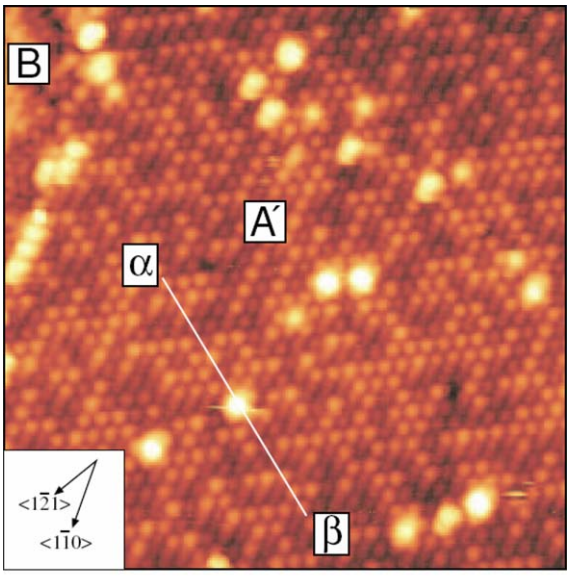

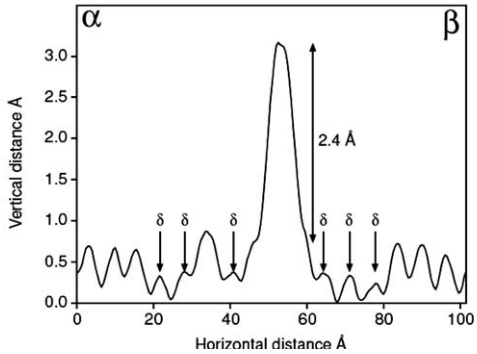

Fig. 14. (a) 200×200 Å^2 constant current (1.97 V, 0.98 nA) STM image of Fe_3O_4 (111) following exposure to 2.0×10^{-7} mbarsec of pyridine vapour at 298 K; (b) line profile taken along transect α–β as indicated in (a). The height of a single adsorbed pyridine molecule of ~2.4 Å is indicated, as are the positions of atomic defects (δ) suggested to be Fe vacancies.

The preferential adsorption of pyridine (and of HCOOH) on A′-type surfaces is consistent with a metal-terminated surface, and the relatively low mobility of adsorbates on these surfaces is attributed to the formation of a chemisorbed species. Fig. 15 shows a schematic representation of pyridine adsorbed on A′-type surfaces of Fe_3O_4 (111). Bonding could occur via the donation of an electron from the lone pair on the heteroatom (N) in the pyridine ring to exposed Fe_{tet1} cations. This has also been observed for pyridine adsorption on ZnO (1100) where UPS measurements indicate that both the nitrogen lone pair and the π orbital are involved in the chemisorption (Lüth et al., 1978). This interpretation would explain the relatively weak interaction between the basic pyridine molecule and A surfaces, which are themselves thought to be terminated with basic oxygen sites. As described above (see Figs. 4a and d) A-type surfaces appear to correspond to an A′-type surface with the exposed Fe_{tet1} ions capped by a single oxygen atom. Thus, as in bulk Fe_3O_4, each Fe ion is tetrahedrally coordinated unless it is located directly beneath a point defect.

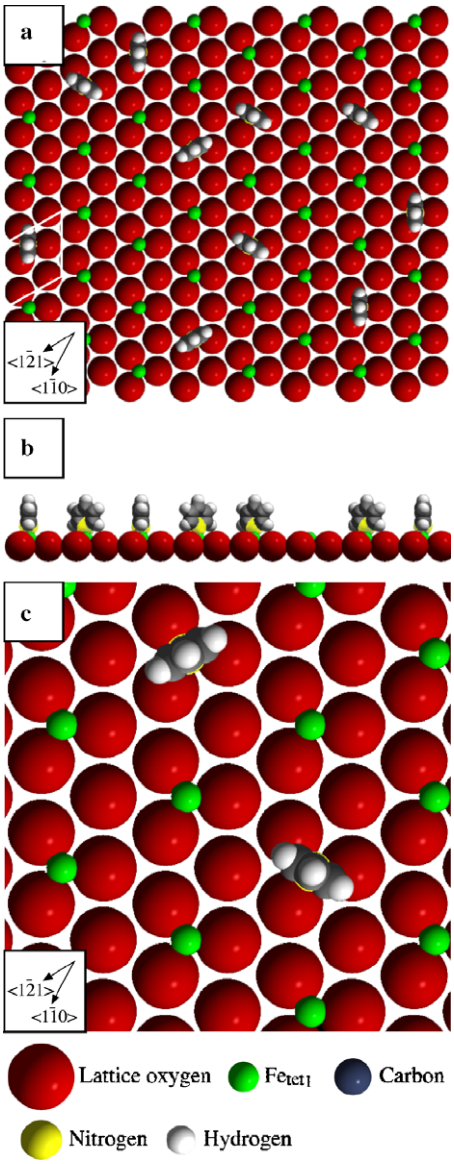

Fig. 15. (a) Top view of a space filling model representing low coverage adsorbed pyridine on an A′-type surface of Fe_3O_4 (111), (b) side view, (c) top view magnified.

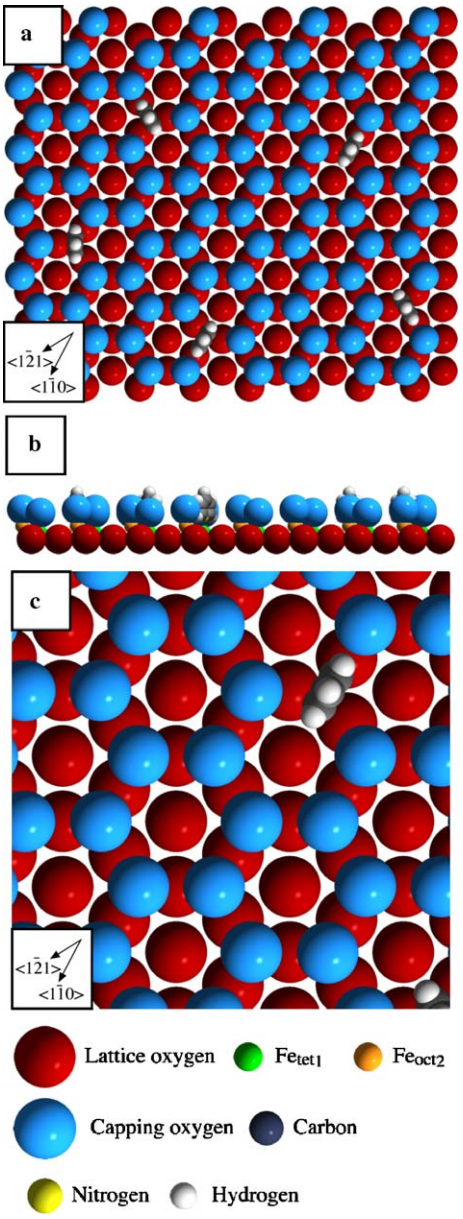

Fig. 16. (a) Top view of a space filling model representing low coverage adsorbed pyridine on a B-type surface of Fe_3O_4 (111), (b) side view, (c) top view magnified.

As noted above, it is also proposed in contrast to previous authors (Lennie et al., 1996), that termination B exposes 1/2 monolayer of oxygen atoms capping 1/2 monolayer of Fe ions over a close-packed oxygen layer. Our experiments indicate that active sites for adsorption on B-type surfaces would be restricted entirely to point defects, as illustrated in Fig. 16. This observation also suggests that we are dealing with an oxygen-terminated surface. On a "perfect" defect-free surface, the average coordination of Fe is tetrahedral. This is consistent with photoelectron diffraction (PED) data obtained from thin film Fe_3O_4 (111) grown on a Pt (111) substrate (Condon et al., 1995), where the authors assert that it is energetically favourable for the underlying oxygen plane to relax outward by 41.7% with respect to the corresponding bulk bond length, exchanging sequence with the overlying Fe layer. This type of surface structure is very similar to that proposed here for a B-type surface, a surface which would be oxygen terminated. The same authors note that the outward relaxation of the topmost oxygen plane is accompanied by strong relaxations of the next three interlayer spacings. Such relaxations could lead to step heights on surfaces observed here that are inconsistent with the separation of specific atomic planes in bulk Fe_3O_4.

3.3. Exposure to carbon tetrachloride

Fig. 17a is a 150×150 Å^2 STM image of a clean Fe_3O_4 (111) surface showing both an A′ and a B surface and Fig. 17b is an STM image of the same area obtained

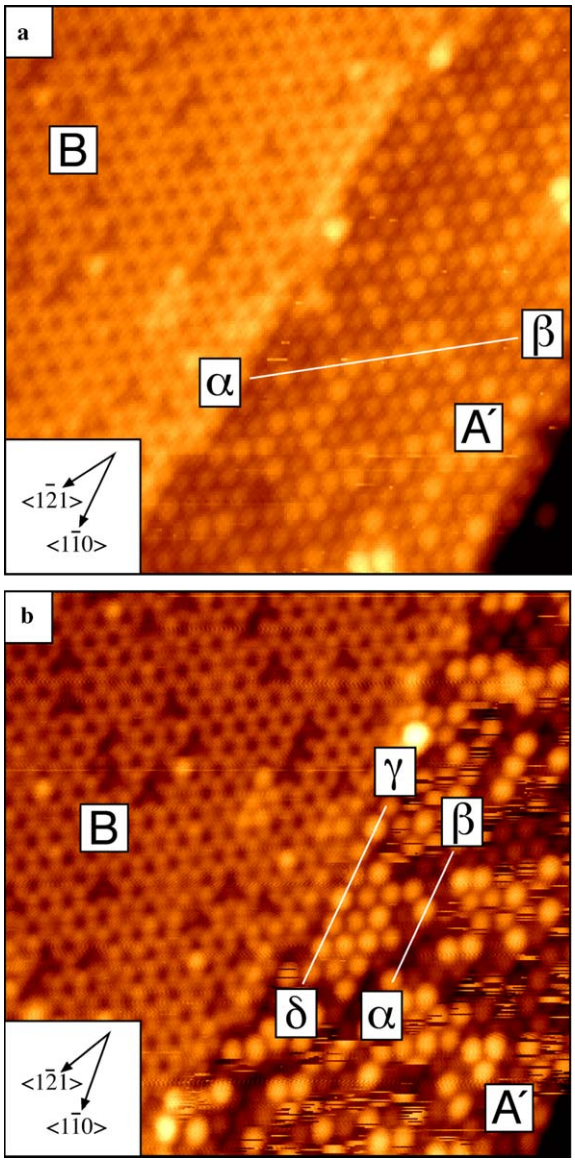

Fig. 17. 150×150 Å^2 constant current (1.97 V, 0.96 nA) STM images of Fe_3O_4 (111) both (a) before and (b) after exposure to 2.0×10^{-6} mbarsec of CCl_4 vapour at 298 K. Line profiles taken along transects α–β indicated in (a) and α–β and γ–δ in (b) are shown in Fig. 18.

following exposure to 2.0×10^{-6} mbarsec of CCl_4 vapour at 298 K. The surface shows adsorption related features imaged as immobile, round-shaped, and bright, and with a number imaged as "blurs" that appear to have a "scratched" or fragmentary shape. It is suggested that, as with formic acid and pyridine, such "blurred" or fragmentary features are mobile at the surface during imaging. In the case of pyridine adsorption on rutile TiO_2 (110), both a mobile species and an immobile species exist and the former is attributed to a physisorbed species, whilst the latter is attributed to a chemisorbed species (Suzuki et al., 1998a, 1999).

In contrast to formic acid and pyridine, exposure of Fe_3O_4 (111) to CCl_4 vapour results in generation of both mobile and immobile adsorbate populations that coexist on the same A′-type surface., There is no evidence for any adsorbate interaction with either B-type (see Fig. 17b) or, as discussed later, A-type surfaces (see Fig. 23). We believe that these are the first atomic resolution observations showing both mobile reaction intermediates and immobile reaction products on an iron oxide surface. Despite the lack of direct chemical information from STM experiments, it is possible to interpret our observations with the help of earlier temperature programmed desorption (TPD) and XPS investigations of CCl_4 adsorption on Fe_3O_4 (111) surfaces (Abib et al., 2002, 2003a). Abib et al. (2002) have investigated the interaction of CCl_4 with a Fe_3O_4 (111) selvage formed on a α-Fe_2O_3 (0001) substrate using TPD analysis. A complex series of spectra result when the temperature of the crystal is increased, following exposure to 2.0×10^{-6} mbarsec of CCl_4 vapour at 100 K. This observation is in itself suggestive of a "rich, site-dependant chemistry" (Abib et al., 2002). The authors propose that the surface reactivity of CCl_4 on Fe_3O_4 (111) can be summarised according to the following equations:

$$CCl_4(g) \underset{100K}{\longrightarrow} CCl_4(ads) \longrightarrow CCl_4(g) \quad (1)$$

$$CCl_4(g) \underset{100K}{\longrightarrow} CCl_2(ads) + 2Cl(ads) \quad (2)$$

$$\rightarrow CCl_4(g) \quad (2a)$$

$$\rightarrow \frac{1}{2}C_2Cl_4(g) + 2Cl(ads) \quad (2b)$$

$$\rightarrow OCCl_2(g) + 2Cl(ads) \quad (2c)$$

$$\rightarrow FeCl_2(g) + CCl_2(ads) \quad (2d)$$

Eq. (1) describes the adsorption and subsequent desorption of molecular CCl_4, either from a multilayer of CCl_4 ice that forms on the substrate at 100 K, or from unreactive sites on the surface itself (Abib et al., 2002). Both processes can be distinguished in TPD spectra, the former occurring at 167 K and the latter at 209 K. In contrast, Eq. (2) represents the dissociative adsorption of CCl_4, which has been shown to occur spontaneously on Fe_3O_4 (111) at 100 K (Abib et al., 2003a). The dissociation of an individual CCl_4 molecule results in the adsorption of CCl_2 and 2Cl at the surface. Eqs. (2a)–(2c) describe the recombinative desorption of CCl_4, the associative desorption of C_2Cl_4, and oxygen abstraction and the desorption of phosgene gas.

The final reaction shown above represents the desorption of $FeCl_2$ (Eq. (2d)) at temperatures in excess of 820 K. A later XPS study has revealed that the conversion of iron monochloride to iron dichloride occurs within a temperature range of 450–820 K (Abib et al., 2003a), indicating that Cl is mobile on Fe_3O_4 (111) surfaces in this temperature range. It is unlikely that the mobile species evident in Fig. 17b is Cl, since the image was obtained at 298 K. On the basis of such arguments, neither CCl_4 nor C_2Cl_4 can be discounted as mobile sorbates, since the desorption of these products continues until ~300 and ~380 K, respectively. However, reaction pathways leading to the desorption of

either CCl_4 or C_2Cl_4 are relatively minor compared to that leading to $OCCl_2$ desorption (Abib et al., 2002). The same authors have estimated $OCCl_2$–CCl_4–C_2Cl_4 ratios of 34:4:1. Furthermore, the onset of $OCCl_2$ desorption at 282 K corresponds exactly to the maxima of both CCl_4 and C_2Cl_4 desorption. The authors note that the relative proportions of both CCl_4 and C_2Cl_4 desorbed is further reduced, apparently as a result of the onset of $OCCl_2$ desorption (Abib et al., 2002). Thus, it follows that at 298 K, $OCCl_2$ is the dominant desorbing species, which means that the CCl_2 intermediate must be mobile at the surface since this species is a prerequisite of phosgene desorption. The detection of surface bound CCl_2 but not $OCCl_2$ using XPS at 100 K indicates that the formation of the latter is a two-step process, with the formation of a carbonyl bond involving the CCl_2 intermediate and a surface oxygen requiring thermal activation (Abib et al., 2003a). It is proposed that the mobile population of adsorbates seen in Fig. 17b represents CCl_2 intermediates that are bound initially at surface Fe sites. At 298 K, the molecule should be capable of forming a carbonyl bond, extracting O from the substrate and desorbing as $OCCl_2$. It is also proposed that the immobile adsorbates evident in Fig. 17b are Cl atoms, bound atop surface Fe_{tet1} sites. This interpretation is supported by XPS data suggesting that Cl mobility is confined to the temperature range ~450–820 K, when $FeCl_2$ is observed as a desorbing species (Abib et al., 2003a). In addition, STM data presented by Rim et al. (2003, 2004) support this interpretation. The authors show that the onset of extensive oxygen abstraction/phosgene desorption from Fe_3O_4 (111) is suppressed below ~280 K and that, consequently, the adsorption of Cl atoms produced by the dissociation of CCl_4 occurs atop Fe_{tet1} ions. Although it is important to note that the TPD studies conducted by Abib et al., 2002 do not yield data related to termination specific reactions, the authors did use their TPD data to estimate the proportion of surface sites that are active for CCl_4 dissociation. Approximately 73% of CCl_4 molecules in direct contact with the surface actually did dissociate, and it was proposed that the remaining 27% were adsorbed

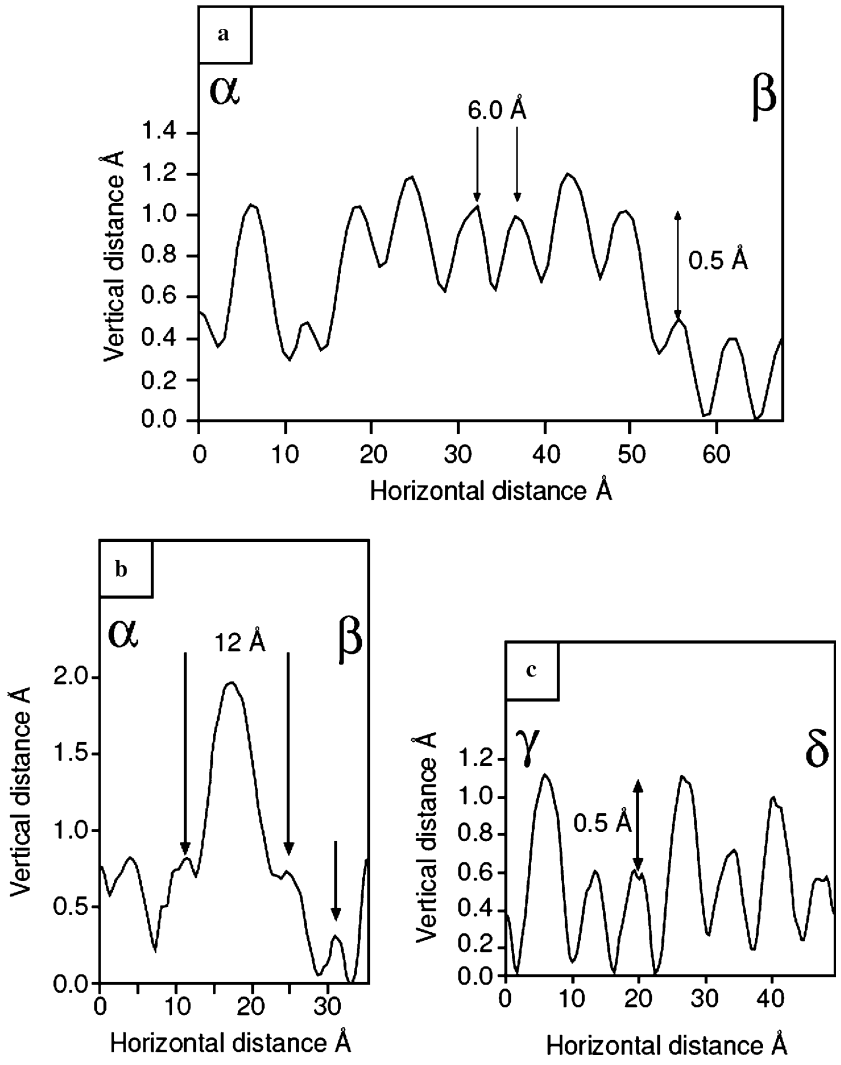

Fig. 18. (a–c) are line profiles taken along transects α–β in Fig. 17(a), and α–β and γ–δ in Fig. 17(b), respectively.

molecularly on oxygen-terminated regions of the Fe_3O_4 (111) surface. This estimate is broadly consistent with our STM observations that indicate approximately 25% of the exposed surface is oxygen terminated, although this value may vary with the precise conditions employed during sample preparation.

Fig. 18a is a line profile taken along the transect marked α–β in Fig. 17a. The 6.0 Å lateral separation of features on the clean A′-type surface is evident, as is the presence of protrusions that are ~0.5 Å higher than the majority of protrusions comprising the surrounding terrace. The physical basis for such height variation on a clean A′ terrace is unknown at the present time, although it is clear from repeated scanning that the features are immobile at room temperature and are imaged in a reproducible manner in successive scans. One possibility is that this observed difference in the tunneling characteristics of bright protrusions reflects the presence of both Fe^{2+} and Fe^{3+} at the surface. Unfortunately, numerous attempts to obtain atomic resolution images at negative bias voltages have proved unsuccessful. Figs. 18b and c are line profiles taken along the transects marked α–β and γ–δ in Fig. 17b. The first of these profiles shows that a single immobile adsorption related feature is associated with a single protrusion in the underlying substrate, with the former sitting atop of the latter. Furthermore, adsorption related features yield a measured height of ~1.2 Å, and a width (FWHM) of ~8 Å. The lateral registry of adsorbates with atomic rows in the substrate again offers support to the proposal that A′ surfaces are terminated by 1/4 monolayer of Fe_{tet1} ions rather than 3/4 monolayer of Fe_{oct1} ions. If the latter were the case, and each substrate protrusion represented a trimer of Fe ions, one would expect to observe at least one example of a substrate protrusion that is associated with two, or even three, adsorption related features. However, no such observations were made during the present investigation. Fig. 18c shows that the height difference of 0.5 Å, apparent amongst substrate protrusions and also seen in Fig. 18a, is preserved on the adsorbate covered surface.

Fig. 19 is a 200×200 Å^2 STM image of the same area imaged in Fig. 17 but obtained following exposure to a further 4.0×10^{-6} mbarsec of CCl_4 vapour at 298 K, giving a total exposure of 6.0×10^{-6} mbarsec. It can be seen that the A′ surface is almost entirely saturated with adsorbates, whereas the adjacent B surface remains unaffected by exposure to the CCl_4 vapour. In this image, only one population of immobile adsorbates is evident on the A′ surface, all adsorption related features appear round in shape and immobile during scanning. These features are thought to be individual chlorine atoms that are produced in a ratio of 2:1 with respect to the CCl_2 intermediate as a result of the dissociative adsorption of individual CCl_4 molecules. This process is illustrated schematically in Fig. 20. Each proposed configuration is consistent with the 2:1 ratio of Cl and CCl_2 determined from previous TPD studies (Abib et al., 2002) and the incorporation of nearest-neighbour Fe_{tet1} sites. Fig. 19 shows that the second population of

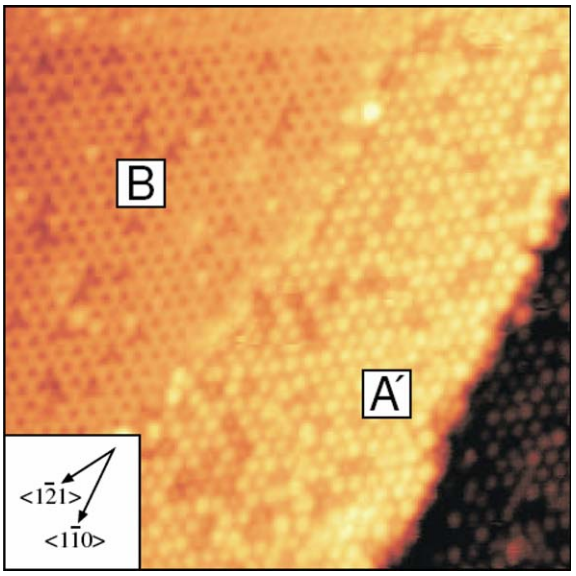

Fig. 19. 200×200 Å^2 constant current (1.97 V, 0.96 nA) STM image of the same region of the Fe_3O_4 (111) surface presented in Fig. 17, following exposure to a total of 6.0×10^{-6} mbarsec of CCl_4 vapour at 298 K.

mobile adsorbates, imaged as "scratch" shaped fragments in Fig. 17b, is absent. It is not clear if this is because they have been driven from the scan area by the tip, although repeatedly increasing the scan size around the area imaged shows these areas to be devoid of mobile adsorbates. A more plausible explanation is that the mobile species, thought to be CCl_2, adsorbs initially at a Fe site as suggested by earlier XPS experiments (Abib et al., 2003a).

The second-step of the reaction, leading to the formation of $OCCl_2$, would involve the migration of the CCl2 intermediate to an adjacent uncapped oxygen site. Such sites are clearly present within the (1×1) surface unit cell of A′ surfaces (Fig. 4e). The formation of a carbonyl bond with a substrate oxygen and concomitant extraction of surface oxygen and desorption of phosgene occurs spontaneously at 298 K (Abib et al., 2003a), although $OCCl_2$ desorption does not reach a maximum until ~320 K. The process of oxygen extraction and phosgene desorption is represented schematically in Fig. 20b. The temperature of 298 K employed in our experiments may be such that the CCl_2 intermediate has a finite residence time at surface Fe sites. Step two in the formation of $OCCl_2$, involving migration of the CCl_2 intermediate, is also thought to occur spontaneously, giving rise to the adsorbates imaged as "scratched" features (Fig. 17b). The absence of mobile adsorbates in Fig. 19 may be because further exposure to CCl_4 vapour shifts the equilibrium described by Eq. (2c) to the right, leading to increased phosgene desorption. This, in turn, could lead to the reduction of the substrate as increasing numbers of threefold oxygen vacancies are formed due to phosgene desorption. In keeping with previous authors (Camillone et al., 2002; Rim et al., 2003, 2004), it is proposed that reactive oxygen sites for CCl_2 adsorption at 298 K occur at the position marked "x" in

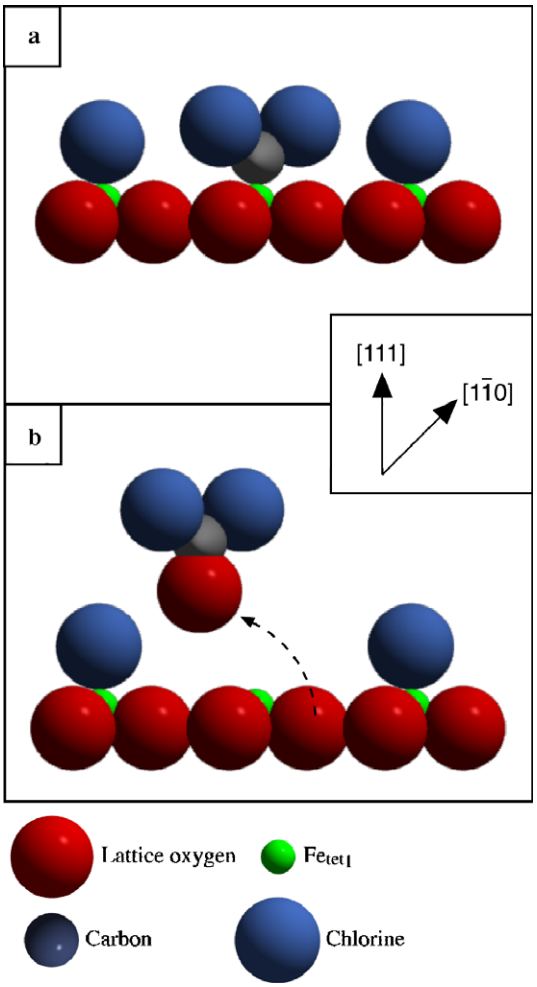

Fig. 20. (a) Schematic representation of the initial adsorption geometry of CCl_4 fragments (2Cl and CCl_2) on A′-type surfaces at 100 K; (b) depicts phosgene desorption, which occurs spontaneously following the formation of a carbonyl bond between the CCl_2 intermediate and an uncapped oxygen atom in the substrate. Crystallographic directions of the substrate are indicated.

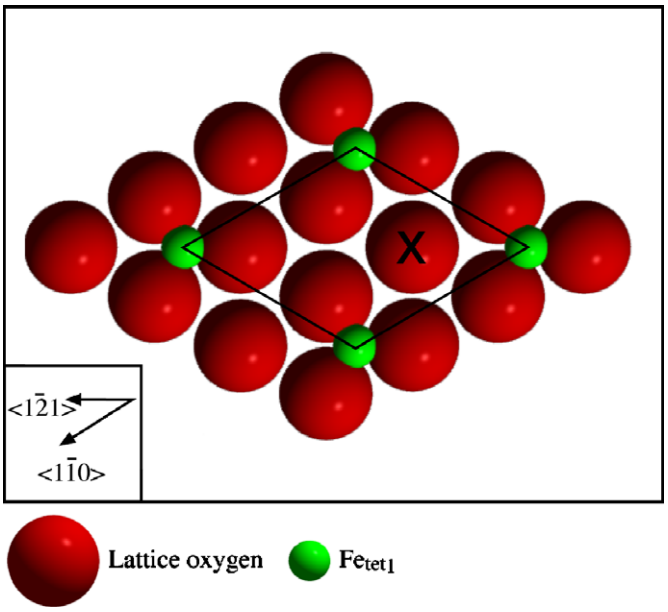

Fig. 21. Schematic representation of the (1×1) surface unit cell of an A′-type termination of Fe_3O_4 (111). Oxygen atoms in the site designated "x" expose a dangling bond normal to the surface and exhibit an electron density of 0.75. Oxygen ions in this position are not bound to Fe_{tet1} ions in the overlying cation plane and are thus more reactive than other oxygen sites for carbonyl formation with a CCl_2 intermediate. The (1×1) unit cell and crystallographic directions of the substrate are indicated.

Fig. 21. Such sites serve to stabilise CCl_2 species prior to phosgene desorption. Oxygen atoms that occupy this particular position are not bonded to Fe_{tet1} ions that comprise the overlying atomic plane. Simple electron distribution arguments suggest that the site marked "x" contains ~0.75 electrons. In contrast, other oxygen sites within the (1×1) surface unit cell that are bound to overlying Fe_{tet1} ions contain ~0.5 electrons (Camillone et al., 2002). Hence, the polarizing effect of iron, increased electron density, and vertical dangling bond associated with the oxygen atom designated "x" in Fig. 20, could facilitate the heterolytic cleavage of C–Cl bonds in CCl_4 to produce Cl^- by providing the requisite electrons (Camillone et al., 2002). The proposed structure of A′-type surfaces following extensive reaction with CCl_4 vapour at 298 K is illustrated in Fig. 22.

Fig. 23 is a 200×195 Å^2 STM image of a different region of the Fe_3O_4 (111) surface following exposure to 6.0×10^{-6} mbarsec of CCl_4 vapour at 298 K. Here, the A′ surface is almost entirely saturated with bright immobile adsorbates that are attributed to Cl atoms. In contrast, the adjacent A surface exposes a characteristic hexagonal array of bright features, with a relatively high concentration of point and linear defects, but no evidence for adsorbates. This is consistent with the proposal that A-type surfaces are O-terminated. The reason for the absence of adsorbates at defects on A surfaces is unclear, since such sites are thought to expose underlying Fe atoms. It may be that the presence of capping oxygen atoms, surrounding point defects, makes the dissociative adsorption of CCl_4 a sterically unfavourable process.

Fig. 24a is a 500×500 Å^2 STM image obtained following exposure to 6.0×10^{-6} mbarsec of CCl_4 and subsequent flash annealing to 673 K for 3 min. The surface is very different to previous images, exposing intergrown domains of termination A′ and an unknown phase that is resistant to tunneling. Some ordering among the different domains appears evident. It is proposed that these tunneling resistant domains are composed of $FeCl_2$ that crystallises as a result of the desorption of $OCCl_2$, accompanied by the reduction of Fe^{3+} to Fe^{2+} and subsequent reaction with adsorbed Cl. This interpretation is supported by the TPD results of Abib et al. (2002), who observe the transformation of iron monochloride into iron dichloride at temperatures >450 K. The transformation process occurs until the onset of $FeCl_2$ desorption is reached at 820 K. The conversion of one iron and chlorine-bearing phase into another is evidence for the mobility of Cl at the surface between ~450 K and ~820 K. The temperature used during flash

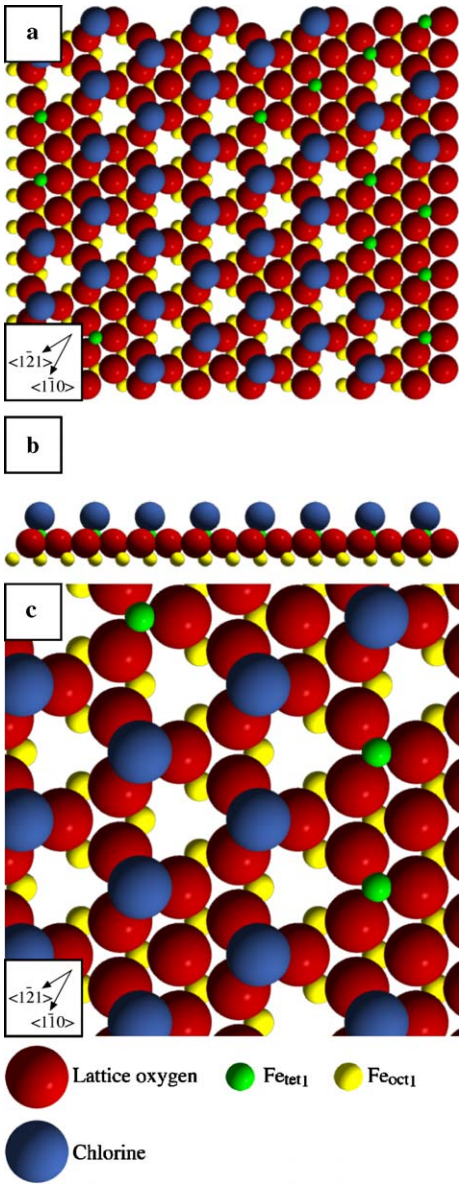

Fig. 22. (a) Top, (b) side, and (c) magnified top view of a schematic representation of an A′-type surface following exposure to CCl_4 vapour at 298 K. Oxygen defects are the result of carbonyl bond formation between the CCl_2 reaction intermediate and oxygen atoms that occupy the position designated "x" in Fig. 21. At 298 K, phosgene desorption is extensive and results in the abstraction of oxygen from the substrate. The underlying oxygen plane is omitted for clarity.

annealing (673 K) lies within this range, and it is proposed that exposure to CCl_4 vapour at 298 K results in the growth of an iron monochloride surface phase on A′ surfaces. This is supported by atomic resolution STM images that confirm the presence of both a majority and a minority Cl population, as observed by Rim et al. (2003, 2004). The majority population is characterised by the association of a single Cl atom atop a single Fe_{tet1} atom on A′-type surfaces. The minority population is characterised by larger, brighter features, several of which are indicated in Fig. 24 using white circles, and occupies positions that correspond

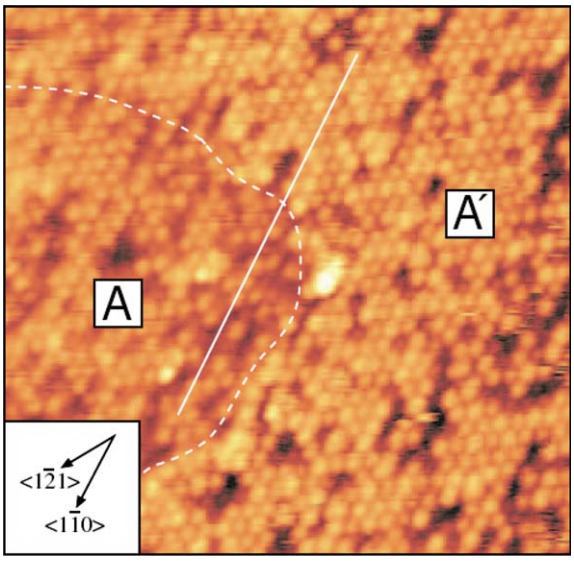

Fig. 23. 200×195 Å^2 constant current (1.93 V, 0.75 nA) STM image of Fe_3O_4 (111) that exposes both an A and an A′ surface, after exposure to 6.0×10^{-6} mbarsec of CCl_4 vapour at 298 K. The boundary between the two surfaces is indicated with the use of a dashed white line. The straight line is used to show the lateral registry of features on either side of the boundary.

to the centers of equilateral triangles defined by the positions of lattice protrusions separated by 6 Å. This position corresponds to a threefold oxygen vacancy site that exposes three underlying Fe_{oct1} ions (see Fig. 22), generated as a result of oxygen abstraction/phosgene desorption. This result is inconsistent with data presented in previous studies (Rim et al., 2003, 2004), who clearly show that flash annealing following room temperature exposure to CCl_4 vapour results in a majority Cl species bound at three-fold oxygen vacancy sites, and a minority population atop Fe_{tet1} ions. The reasons for this subtle variation in adsorbate site occupancy are not understood at present. Fig. 24b is a 200×200 Å^2 STM image of the same region shown in Fig. 24a. The terraces surrounding the tunneling resistant domains that are attributed to $FeCl_2$ are thought to be A′-type surfaces. The bright features ~1.2 Å in height, with widths (FWHM) of 8.0 Å, are thought to reflect the presence of surface bound Cl remaining after the majority of surface bound Cl is desorbed as $OCCl_2$, or incorporated into $FeCl_2$ at temperatures >450 K.

4. Conclusions

Atomic resolution imaging of the (111) surface of magnetite has confirmed the existence of a number of possible terminations related to slices at different levels through the bulk structure. These include previously reported surfaces labeled A, B, and A′. Exposure of these surfaces to three contrasting organic molecules under controlled (UHV) conditions has provided further insights into the structures of these surfaces and their relative reactivities, and revealed a wealth of surface reaction phenomena.

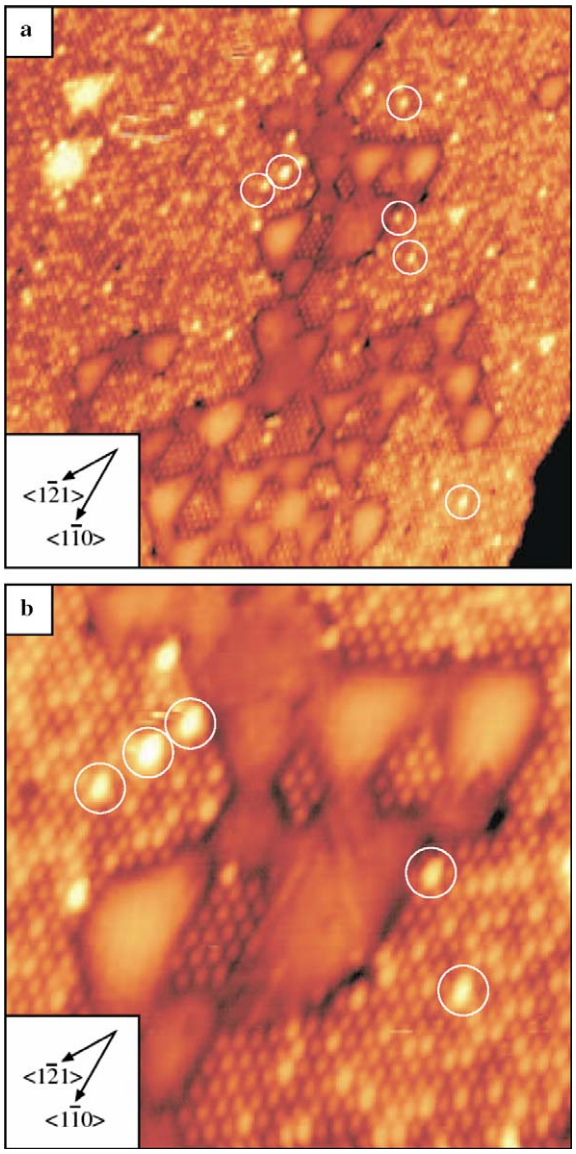

Fig. 24. (a) 500×500 Å^2 and (b) 200×200 Å^2 constant current (1.22 V, 0.96 nA) STM images of Fe_3O_4 (111), obtained following exposure to 6.0×10^{-6} mbarsec of CCl_4 at 298 K and annealing to 673 K for 3 min. White circles indicate the positions of several examples of minority adsorbates located at threefold oxygen vacancy sites.

For all three organic molecules, the A′ surface is most reactive, but reaction behaviour varies significantly between the systems. Bonding to Fe site (A′) surface atoms, or such atoms exposed at defects on the other surfaces, appears to involve a bidentate non-bridging complex in the case of formate (formic acid dissociating on contact with the magnetite surface), but a monodentate linkage via the 'basal' nitrogen atom in the case of pyridine. In both of these systems, a weaker interaction (a 'physisorption') was evident between the intact organic molecule and the oxygen-terminated surface regions of non-defective A and B surfaces. Carbon tetrachloride appears to undergo a series of temperature-dependent dissociation and surface chemical reactions, with sorption of intact CCl_4 molecules at the lowest temperatures, dissociation into CCl_2 and Cl species at around room temperature, and removal of surface O to form $OCCl_2$ molecules and then Fe to form $FeCl_2$ at successively higher temperatures. At around room temperature, strongly bonded Cl atoms co-exist with weakly held CCl_2 molecules. Hence, this system appears to offer the first example in an iron oxide system with 'chemisorbed' and 'physisorbed' species on the same type of surface.

Acknowledgments

The support of both the Natural Environment Research Council and the Engineering and Physical Sciences Research Council in funding this research is gratefully acknowledged. Dr Paul Wincott is thanked for his advice on aspects of the work.

Associate editor: Carrick M. Eggleston

References

Abib, K., Camillone, N., Fitts, J.P., Rim, K.T., Flynn, G.W., Joyce, S.A., Osgood, R.M., 2002. CCl_4 chemistry on the magnetite selvedge of single-crystal hematite: competitive surface reactions. *Surf. Sci.* **497**, 127–138.

Abib, K., Mullins, D.R., Totir, G., Camillone, N., Fitts, J.P., Rim, K.T., Flynn, G.W., Osgood, R.M., 2003a. Dissociative adsorption of CCl_4 on the Fe_3O_4 (111)-(2×2) selvedge of α-Fe_2O_3 (0001). *Surf. Sci.* **524**, 113–128.

Abib, K., Totir, G.G., Fitts, J.P., Rim, K.T., Mueller, T., Flynn, G.W., Joyce, S.A., Osgood Jr., R.M., 2003b. Chemistry of CCl_4 on Fe_3O_4 (111)-(2×2) surfaces in the presence of adsorbed D_2O studied by temperature programmed desorption. *Surf. Sci.* **537**, 191–204.

Ahdjoudj, J., Minot, C., 1997. A theoretical study of HCO_2H adsorption on TiO_2 (110). *Catal. Lett.* **46**, 83–91.

Ahdjoudj, J., Martinsky, C., Minot, C., Van Hove, M.A., Somorjai, G.A., 1999. Theoretical study of the termination of the Fe_3O_4 (111) surface. *Surf. Sci.* **443**, 133–153.

Barbieri, A., Weiss, W., Van Hove, M.A., Somorjai, G.A., 1994. Magnetite Fe_3O_4 (111)-Surface structure by LEED crystallography and energetics. *Surf. Sci.* **302**, 259–279.

Bates, S.P., Kresse, G., Gillan, M.J., 1998. The adsorption and dissociation of ROH molecules on TiO_2 (110). *Surf. Sci.* **409**, 336–349.

Binnig, G., Rohrer, H., 1982. Scanning tunneling microscopy. *Helv. Phys. Acta* **55**, 726–735.

Bullister, J.L., Wisegarver, D.P., 1998. The solubility of carbon tetrachloride in water and seawater. Deep-Sea Research, Part I. *Oceanogr. Res. Pap.* **45**, 1285–1302.

Camillone, N., Abib, K., Fitts, J.P., Rim, K.T., Flynn, G.W., Joyce, S.A., Osgood, R.M., 2002. Surface-termination-dependence of the reactivity of single crystal hematite with CCl_4. *Surf. Sci.* **511**, 267–282.

Canter, L.W., Sabatini, D.A., 1994. Contamination of public groundwater supplies by superfund sites. *Int. J. Environ. Stud.* **46**, 35–57.

Chambers, S.A., Thevuthasan, S., Kim, Y.J., Herman, G.S., Wang, Z., Tober, E., Ynzunza, R., Morais, J., Peden, C.H.F., Ferris, K., Fadley, C.S., 1997. Chemisorption geometry of formate on TiO_2 (110) by photoelectron diffraction. *Chem. Phys. Lett.* **267**, 51–57.

Condon, N.G., Leibsle, F.M., Lennie, A.R., Murray, P.W., Vaughan, D.J., Thornton, G., 1995. Biphase ordering of iron oxide surfaces. *Phys. Rev. Lett.* **75**, 1961–1964.

Domen, K., Akamatsu, N., Yamamoto, H., Wada, A., Hirose, C., 1993. Infrared invisible sum frequency generation study of HCOOH on an MgO (001) surface. *Surf. Sci.* **289**, 468–472.

Fellows, R.A., Lennie, A.R., Raza, H., Pang, C.L., Thornton, G., Vaughan, D.J., 2000. Fe_3O_4 (111) formation on a reduced α-Fe_2O_3 (1123) substrate: a low energy electron diffraction and scanning tunnelling microscopy study. *Surf. Sci.* **445**, 11–17.

Fetzner, S., 1998. Bacterial degradation of pyridine, indole, quinoline, and their derivatives under different redox conditions. *Appl. Microbiol. Biotechnol.* **49**, 237–250.

Gercher, V.A., Cox, D.F., 1994. Formic acid decomposition on SnO_2 (110). *Surf. Sci.* **312**, 106–114.

Hale, R.C., Aneiro, K.M., 1997. Determination of coal tar and creosote constituents in the aquatic environment. *J. Chromatogr. A.* **774**, 79–95.

Happell, J.D., Wallace, D.W.R., 1998. Removal of atmospheric CCl_4 under bulk aerobic conditions in groundwater and soils. *Environ. Sci. Technol.* **32** (9), 1244–1252.

Henderson, M.A., 1997. Complexity in the decomposition of formic acid on the TiO_2 (110) surface. *J. Phys. Chem. B.* **101**, 221–229.

Idriss, H., Lusvardi, V.S., Barteau, M.A., 1996. Two routes to formaldehyde for formic acid on TiO_2 (001) surfaces. *Surf. Sci.* **348**, 39–48.

Iwasawa, Y., Onishi, H., Fukui, K.-I., Suzuki, S., Sasaki, T., 1999. The selective adsorption and kinetic behaviour of molecules on TiO_2 (110) observed by STM and NC-AFM. *Faraday Discuss.* **114**, 259–266.

Joseph, Y., Kuhrs, C., Ritter, M., Weiss, W., 1999a. Adsorption of water on Fe_3O_4 (111) studied by photoelectron and thermal desorption spectroscopy. *Surf. Sci.*, 114–118.

Joseph, Y., Kuhrs, C., Ritter, M., Weiss, W., 1999b. Adsorption of water on FeO (111) and Fe_3O_4 (111): identification of active sites for dissociation. *Chem. Phys. Lett.* **314**, 195–202.

Khalil, M.A.K., Rasmussen, R.A., 1989. The potential of soils as a sink of chlorofluorocarbons and other man-made chlorocarbons. *Geophys. Res. Lett.* **16**, 679–682.

Kim, Y.J., Westphal, C., Ynzunza, R.X., Wang, Z., Galloway, H.C., Salmeron, M., Van Hove, M.A., Fadley, C.S., 1998. The growth of iron oxide films on Pt (111): a combined XPD, STM, and LEED study. *Surf. Sci.* **416**, 68–111.

Klick, S., 1992. Seasonal variations of biogenic and anthropogenic halocarbons in seawater from a costal site. *Limnol. Oceanogr.* **37**, 1579–1585.

Lennie, A.R., Condon, N.G., Leibsle, F.M., Murray, P.W., Thornton, G., Vaughan, D.J., 1996. Structures of Fe_3O_4 (111) surfaces observed by scanning tunneling microscopy. *Phys. Rev. B.* **53**, 10244–10253.

Lindsay, R., Michelangeli, E., Daniels, B.G., Ashworth, T.V., Limb, A.J., Thornton, G., Gutierrez-Sosa, A., Lizzit, S., 2002. Impact of defects on the surface chemistry of ZnO (0001)-O. *J. Am. Chem. Soc.* **124**, 7117–7122.

Lüth, H., Rubloff, G.W., Grobman, W.D., 1978. Chemisorption of organic molecules on ZnO (1100) surfaces: C_5H_5N, $(CH_3)_2CO$ and $(CH_3)_2SO$. *Surf. Sci.* **74**, 365–372.

Montzka, S.A., Butler, J.H., Myers, R.C., Thompson, T.M., Swanson, T.H., Clarke, A.D., Lock, L.T., Elkins, J.W., 1996. Decline in the tropospheric abundance of halogen from halocarbons: implications for stratospheric ozone depletion. *Science* **272**, 1318–1322.

Ohta, K., Ogawa, H., Mizuno, T., 2002. Abiological formation of formic acid on rocks in nature. *App. Geochem.* **15**, 91–95.

Onishi, H., Iwasawa, Y., 1994a. Observation of anisotropic migration of adsorbed organic species using nanoscale patchworks fabricated with a scanning tunneling microscope. *Langmuir* **10**, 4414–4416.

Onishi, H., Iwasawa, Y., 1994b. Removal of adsorbed organic molecules with scanning tunneling microscope: formate anions on TiO_2 (110) surface. *Jpn. J. App. Phys.* **33**, L1338–L1341.

Onishi, H., Iwasawa, Y., 1994c. STM-imaging of formate intermediates on a TiO_2 (110) surface. *Chem. Phys. Lett.* **226**, 111–114.

Petrie, W.T., Vohs, J.M., 1991a. Application of HREEL spectroscopy to characterize adsorbates on an insulating metal oxide: carboxylates on MgO (100). *Surf. Sci. Lett.* **259**, L750–L756.

Petrie, W.T., Vohs, J.M., 1991b. An HREELS investigation of the adsorption and reaction of formic acid on the (0001)-Zn surface of ZnO. *Surf. Sci.* **245**, 315–323.

Peyerimhoff, S.D., 1967. Relationships between AB2 and HnAB2 molecular spectra and geometry: accurate self-consistent field molecular orbital and configuration interaction calculations for various states of $HCOO^-$. *J. Chem. Phys.* **47**, 349–359.

Preuss, E., Krahl-Urban, B., Butz, R., 1974. *Laue Atlas*. Wiley, New York.

Rim, K.T., Fitts, J.P., Muller, T., Adib, K., Camillone, N., Joyce, S.A, Osgood, R.M., Flynn, G.W. 2002. STM studies of iron oxide surfaces: termination of a Fe_3O_4 (111) surface and reaction with carbon tetrachloride. Abstracts of Papers, 223rd American Chemical Society Meeting.

Rim, K.T., Fitts, J.P., Muller, T., Adib, K., Camillone, N., Osgood, R.M., Joyce, S.A., Flynn, G.W., 2003. CCl_4 chemistry on the reduced selvedge of a α-Fe_2O_3 (0001) surface: a scanning tunneling microscopy study. *Surf. Sci.* **541**, 59–75.

Rim, K.T., Muller, T., Fitts, J.P., Adib, K., Camillone, N., Osgood, R.M., Batista, E.R., Friesner, R.A., Joyce, S.A., Flynn, G.W., 2004. Scanning tunneling microscopy and theoretical study of competitive reactions in the dissociative chemisorption of CCl_4 on iron oxide surfaces. *J. Phys. Chem. B* **108**, 16753–16760.

Ritter, M., Weiss, W., 1999. Fe_3O_4 (111) surface structure determined by LEED crystallography. *Surf. Sci.* **432**, 81–94.

Shaikhutdinov, S.K., Ritter, M., Wang, X.G., Over, H., Weiss, W., 1999. Defect structures on epitaxial Fe_3O_4 (111) films. *Phys. Rev. B* **60**, 11062–11069.

Shaikhutdinov, S.K., Weiss, W., Schlogl, R., 2000. Interaction of potassium with Fe_3O_4 (111) at elevated temperatures. *App. Surf. Sci.* **161**, 497–507.

Shimizu, S., Wantanabe, N., Kataoka, T., Shoji, T., Abe, N., Morishita, S., Ichimura, H., 1993. Pyridine and pyridine derivatives. In: Elvers, B., Hawkins, S., Russy, W., Schulz, G. (Eds.), *Ullmann's Encyclopedia of Industrial Chemistry*, vol. A22. VCH Weinheim, New York, pp. 399–430.

Silva, S.L., Patel, A.A., Pham, T.M., Leibsle, F.M., 1999. Scanning tunneling microscopy studies of methoxy and formate on Cu (110) surfaces resulting from reactions with methyl formate, methanol and formic acid. *Surf. Sci.* **441**, 351–365.

Suzuki, S., Yamaguchi, Y., Onishi, H., Fuhui, K.-I., Sasaki, T., Iwasawa, Y., 1998a. STM visualization of site-specific adsorption of pyridine on TiO_2 (110). *Catal. Lett.* **50**, 117–123.

Suzuki, S., Yamaguchi, Y., Onishi, H., Sasaki, T., Fukui, K.-I., Iwasawa, Y., 1998b. Study of pyridine and its derivatives adsorbed on a TiO_2 (110)-(1 × 1) surface by means of STM, TDS, XPS and MD calculation in relation to surface acid-base interaction. *J. Chem. Soc. Farad. Trans.* **94**, 161–166.

Suzuki, S., Onishi, H., Sasaki, T., Fukui, K.-I., Iwasawa, Y., 1998c. Identification of individual 4-methylpyridine molecules physisorbed and chemisorbed on TiO_2 (110)-(1 × 1) surface by STM. *Catal. Lett.* **54**, 177–180.

Suzuki, S., Onishi, H., Fukui, K.-I., Iwasawa, Y., 1999. The condensation reaction of pyridine on TiO_2 (110): STM observation in the presence of the reactant atmosphere. *Chem. Phys. Lett.* **304**, 225–230.

Tanner, R.E., Liang, Y., Altman, E.I., 2002. Structure and chemical reactivity of adsorbed carboxylic acids on anatase TiO_2 (001). *Surf. Sci.* **506**, 251–271.

Voogt, F.C., Fujii, T., Hibma, T., Hoefman, M., Smulders, P.J.M., Wijnja, G.H., Zhang, G.L., Niesen, L., 1996. Growth and properties of epitaxial iron oxide layers. *Hyper. Inter.* **97–98**, 99–108.

Wallace, D.W.R., Beining, P., Putzka, A., 1994. Carbon tetrachloride and chlorofluorocarbons in the South Atlantic Ocean, 19 °S. *J. Geophys. Res. (Oceans)* **99**, 7803–7819.

Wang, L.-Q., Ferris, K.F., Shultz, A.N., Baer, D.R., Engelhard, M.H., 1997. Interactions of HCOOH with stoichiometric and defective TiO_2 (110) surfaces. *Surf. Sci.* **380**, 352–364.

Weiss, W., Barbieri, A., Van Hove, M.A., Somorjai, G.A., 1993. Surface structure determination of an oxide film grown on a foreign substrate: Fe_3O_4 multilayer on Pt (111) identified by low energy electron diffraction. *Phys. Rev. Lett.* **71**, 1848–1851.

Weiss, W., 1997. Structure and composition of thin epitaxial iron oxide films grown onto Pt (111). *Surf. Sci.* **377**, 943–947.

Weiss, W., Ranke, W., 2002. Surface chemistry and catalysis on well-defined epitaxial iron-oxide layers. *Prog. Surf. Sci.* **70**, 1–151.

Wiesendanger, R., 1994. *Scanning Probe Microscopy and Spectroscopy Methods and Applications*. Cambridge Univ. Press, Cambridge.

Zachariasen, W.H., 1940. The crystal structure of sodium formate, $NaHCO_2$. *J. Am. Chem. Soc.* **62**, 1011–1013.